Marine and Petroleum Geology 156 (2023) 106455

Contents lists available at ScienceDirect

Marine and Petroleum Geology

journal homepage: www.elsevier.com/locate/marpetgeo

An optimization method for equivalent bulk permeability of gas shale matrix with crushed samples and re-recognition of the influence of pressure and particle size

Wenbin Jiang [a,b], Lili Ji [a,b,*], Chao Luo [c,d], Mian Lin [a,b,**], Gaohui Cao [a], Fang Hao [e], Zhuo Chen [a,b], Yifan He [c,d]

[a] Institute of Mechanics, Chinese Academy of Sciences, Beijing, 100190, China
[b] School of Engineering Science, University of Chinese Academy of Sciences, Beijing, 100190, China
[c] PetroChina Southwest Oil & Gasfield Company, Chengdu, Sichuan, 610051, China
[d] Shale Gas Research Institute of PetroChina Southwest Oil & Gasfield Company, Chengdu, Sichuan, 610051, China
[e] School of Geosciences, China University of Petroleum, Qingdao, Shandong, 266580, China

ARTICLE INFO

Keywords:
Shale gas
Crushed sample
Matrix permeability
Non-Darcy
Optimization method

ABSTRACT

The pressure decay (or gas expansion) test with crushed samples has been used to evaluate the matrix permeability of shale and other low-permeability rock for many years. However, there still exist uncertainties relating to particle size and equilibrium pressure. The existing late-stage curve fitting method has the advantage of easy calculation, but the assumption that gas enters particles with a single permeability value is not generally applicable for shale samples, and late-stage analysis may lead to underestimation. This study proposes an optimization method to determine the equivalent bulk permeability that ensures the smallest sum of squares of errors between the forward-predicted pressure decay curve and the measure one. Both the optimization and curve fitting method are applied to two shale samples from the Ordovician Wufeng Formation of two wells in the Sichuan Basin, China with improved apparatus and testing procedures. The optimization method is superior to the curve fitting method in the repeatability and regularity on the change of apparent permeability with pressure. A strong linear relationship between apparent permeability and coefficient of compressibility is established between 3 and 12 bars. The variation of permeability with particle size is more diverse than that is commonly understood and might be nonmonotonic, depending on the change of pore structure during crushing. Change of apparent permeability with pressure (non-Darcy feature) is proposed as a criterion of whether pore structure has changed significantly. It is suggested to measure the variation of permeability with pressure and particle size to obtain a more comprehensive understanding of matrix permeability and pore structure.

1. Introduction

Shale gas is typically self-generated and self-stored (Zou et al., 2015, 2016). Due to the low-permeability of shale, gas is in void space which is mainly in nanometer-scale matrix pores and microfractures (Loucks and Reed, 2014; MA et al., 2020; Wu et al., 2020a). On the other hand, artificial fracturing is performed in shale to facilitate economic flow rate from wells. The gas travels through multi-stage channels that include matrix pores, artificial fractures, and the wellbore. Existing researches show that the matrix permeability influences the long-term performance of shale reservoirs, and is an important parameter for the evaluation of reservoir quality and identification of highly productive sweet spots (Cao et al., 2018; Pan and Connell, 2015; Qu et al., 2016).

The methods to measure matrix permeability can be divided into two categories based on the shapes of samples used. The first category consists of pressure pulse decay and gas expansion using regular shapes, such as cubes and cylinders (Cui et al., 2010; Handwerger et al., 2011; Haskett et al., 2013; Heller et al., 2014; Pan et al., 2015; Peng and Loucks, 2016; Yang et al., 2017). The second one is the pressure decay method using crushed samples. For samples without microfractures, it is suitable to use the first method. However, gas-bearing shale always contains microfractures along bedding plane, especially in shales of the

* Corresponding author. Institute of Mechanics, Chinese Academy of Sciences, Beijing, 100190, China.
** Corresponding author. Institute of Mechanics, Chinese Academy of Sciences, Beijing, 100190, China.
E-mail addresses: jilili@imech.ac.cn (L. Ji), linmian@imech.ac.cn (M. Lin).

https://doi.org/10.1016/j.marpetgeo.2023.106455
Received 20 December 2022; Received in revised form 19 July 2023; Accepted 9 August 2023
Available online 11 August 2023

Ordovician Wufeng Formation and the basal Longmaxi Formation in the Sichuan Basin, China. Pressure pulse decay tests of cubic shale samples show that permeability along the bedding plane can be two orders of magnitude larger than those perpendicular to the bedding plane (Cao et al., 2019; Ji et al., 2019; Pan et al., 2015). The existence of microfractures will lead to a larger discrepancy between the measured permeability and the actual matrix permeability. Even with high confining pressure, the influence of microfractures can be reduced, but not eliminated (Cui et al., 2018; Peng and Loucks, 2016). Shale is likely to crumble along microfractures or bedding planes during crushing, and the crushed samples should contain fewer microfractures than the whole rock without crushing. The second kind of method is more likely to obtain the flow characteristic controlled by matrix pores. Although it has the disadvantage that no confined pressure can be applied on the tested samples, neither method can currently satisfy both issues. The crushed-sample method has several other advantages, such as a shorter test time, lower requirements on the shape and size of original samples, and is widely used in shale gas exploration in North American (Cui et al., 2009; Luffel and Guidry, 1992).

The crushed-sample method records the time-varied amount of gas that penetrates into pore space of crushed samples with the initial state that a known amount of gas is outside the particles. The amount of penetrated gas can be calculated by measuring the changes of the value of the pressure transducer mounted to the chamber according to the equation of state. Therefore, it is referred to as the "pressure decay" method or the "gas expansion" method. There are mainly two kinds of algorithms to determine matrix permeability following the above testing procedure. One is embedded in the commercial software provided with a SMP-200 shale matrix permeameter produced by Core Laboratories®. The result is determined through history matching with a reservoir simulator (Chavent et al., 1975; Luffel and Guidry, 1992; Oliver and Chen, 2011). Few details are available in the literature and the algorithm is difficult to evaluate. The second kind of algorithm employs one-dimensional equations in the spherical coordinate system describing the permeation of gas into spherical particles according to Darcy's law (Cui et al., 2009). The permeability can be determined through linear fitting of one variable related to the penetrated gas volume and another variable related to the elapsed time with the approximate analytical solution. Therefore, it is referred to as curve fitting method. Existing research shows that the differences of results determined by history matching and curve fitting algorithms may be larger than one order of magnitude. The pressure decay curve consists of an early-time hyperbolic decay stage and a late-time exponential decay stage. For homogeneous reservoir rocks, permeability determined from these two stages should be close. Considering that the early-time data is likely of poor quality, and the late-time data is more recommended to determine the matrix permeability (Cui et al., 2009; Fisher et al., 2017). For natural heterogeneous or dual porosity rocks, the difference between the curve fitting permeability from the early and the late stage can be larger than one order of magnitude (Achang et al., 2017; Fisher et al., 2017; Peng and Loucks, 2016). The permeability determined with the late-time data might only be able to represent partial, not the whole, of the matrix pore space. The higher permeability determined with the hyperbolic segment might be caused by existence of larger natural pores or sample damage. There is currently a lack of means to judge how much of the hyperbolic segment is worthy of inclusion in the permeability determination and produce an equivalent bulk permeability that can represent the entire pore space more closely.

Moreover, there are also large differences between the determined permeability using crushed samples with different particle sizes (Achang et al., 2017; Civan and Devegowda, 2015). One of possibility is the change of pore structure during crushing. Besides, the variation of permeability with particle size may also be due to the discrepancy between actual particle size and the value that is determined according to the apertures of the screens used. There is also a possibility that is difficult to rule out. Existing understanding of the variation of crushed-sample permeability with particle size is established on the basis of local solutions. The equilibration time is always longer for samples with larger particles as gas has to travel farther. It is unclear that whether the linear segment in the LnFR-time plot of samples with different particle sizes corresponds to the same amount of pore space when multiple-scale porosity coexists. There are currently no effective methods to distinguish these factors.

The aim of this study is to: 1) investigate the differences of goodness of fit and permeability when different time sections are used for analysis to evaluate the uncertainty of curve fitting methods, 2) propose an optimization method to determine a single equivalent permeability based on a modeled pressure decay curve that has the smallest sum of squares of errors (SSE for short) when compared with the measured one, 3) clarify the differences between the variations of permeability with particle size determined by curve fitting and the optimization method, 4) discuss the possibility of variation of permeability with particle size caused by inaccurate particle size determination. The content of this article is arranged as follows: the studied sample, experimental apparatus, testing procedures and analysis methods are introduced in Section 2. Section 3 focuses on the results and discussion and the conclusion follows.

2. Methodology

2.1. Samples and preparation

The samples used in this study are from Ordovician Wufeng Formation in two wells (Fig. 1) located in Sichuan Basin, China. The total organic content (TOC) and percentage of quartz and clay content measured by X-ray Diffraction (XRD) of the samples are listed in Table 1 and Fig. A1.

Large area mosaic SEM imaging technique was utilized to explore the pore space of these samples. It is observed that organic pores are the most developed and contribute mainly to the pore space (Fig. A2 and A3). The specific surface area and pore size distribution of the samples were analyzed with low temperature nitrogen adsorption experiment. There are obvious hysteresis loops between adsorption and desorption branches in the both samples (Fig. A4), indicating that a large number of pores are controlled by narrow-neck-like throats. These two sample have significantly different size distributions of controlling throat (Fig. A5). The elapsed times for the plug samples have difference larger than one order (Fig. A6).

The samples were prepared and tested following the following procedures. Firstly, a number of cylinders with a diameter of 25 mm were cut from a whole-diameter (100 mm) core using an automated air-cooled diamond wire cutting machine to reduce the possibility of fracture generation due to mechanical vibration and water-swelling. The total weight of these cylinders should exceed 120 g, which is twice the maximum accommodated mass of the testing apparatus. The cylindrical samples were dried at 105 °C for over 12 h until their mass remain constant to remove the free and bound water. A Mettler Toledo electronic balance with an accuracy of 1/10,000 was used to measure the mass of the sample in the air (referred to as m_0) and immersed in the anhydrous alcohol (referred to as m_1) with a known density, $\rho_{ethanol}$. The bulk volume, V_{bulk}, can be determined according to the Archimedes buoyancy principle, $V_{bulk} = (m_0 - m_1)/V_{ethanol}$. The bulk density of the sample, ρ_{bulk}, can be calculated as $\rho_{bulk} = m_0/V_{bulk}$. The grain volume of the sample, V_{grain}, was measured with a self-developed matrix permeameter and porosimeter. Then the porosity was calculated as $\varphi_{cylinder} = (V_{bulk} - V_{grain})/V_{bulk} \times 100\%$. The cylindrical samples were then crushed carefully with a jaw crusher to produce as many coarse particles as possible. About 60 g of particles were sieved between 4 and 8 Mesh screens (referred to as 4–8 Mesh sample) and dried under 105 °C for over 6 h until the mass remain static. This sample was loaded into the matrix permeameter and porosimeter to measure porosity and

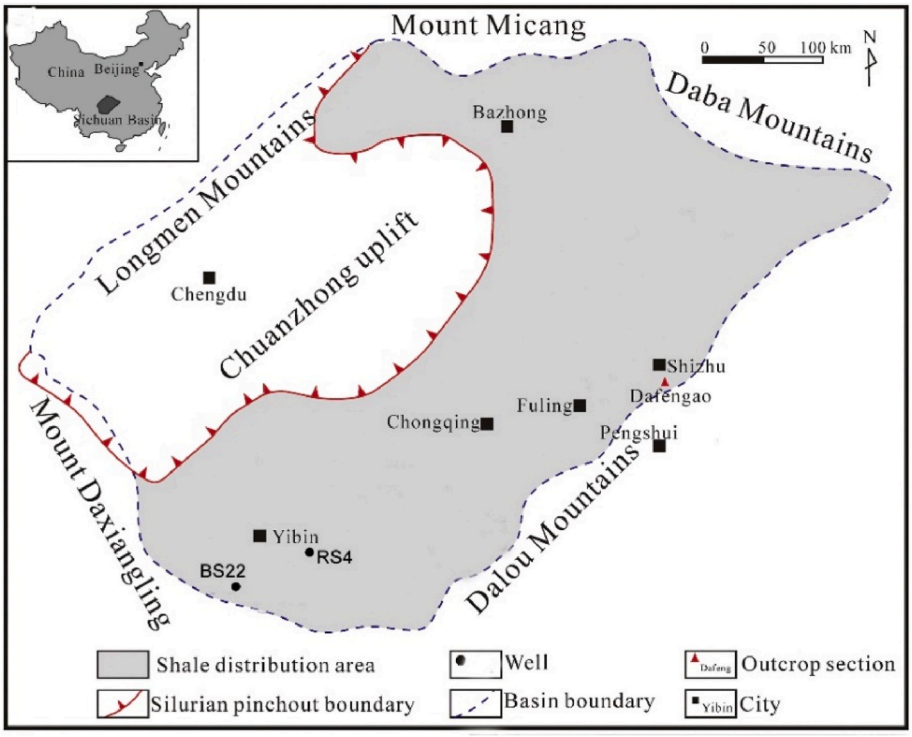

Fig. 1. Location of the sampled wells.

Table 1
The characteristic parameters of the studied samples.

	Depth (m)	Formation	TOC (%)	Quartz (%)	Clay (%)	ρ_{bulk} (g/cm^3)	$\varphi_{cylinder}$ (%)
BS22-45JX	4335.7	Wufeng	5.8	30	21	2.55	2.80
RS4-35JX	3845.64	Wufeng	4.6	48	13	2.49	4.90

permeability. After that, the tested and residual particles were crushed and sieved between 8 and 12, 12 and 16 and 16 and 20 Mesh screens (referred to as 8–12, 12–16 and 16–20 Mesh samples, respectively), and the corresponding porosity and permeability were measured consecutively (Fig. 2). The particles were also crushed to a finer size, sieved between 20 and 28 Mesh screens and tested. However, the pressure decay was too fast and there are too few valid data points, therefore, the 20–28 Mesh sample was not included in the discussion section.

2.2. Experimental apparatus

The in-house matrix permeameter and porosimeter (Fig. 3) used in this study consist of a reference chamber, a sample chamber, stainless steel gas circuits, air-operated valves, a vacuum pump, a helium cylinder, a thermostat air bath, etc. The thermostat air bath ensures that the temperature in the apparatus stays between 32.9 °C and 33.1 °C. The pressure transducer has an accuracy of 0.1%FS and has a range of 25 bar, and the resolution is 60Pa. The sampling interval can be as low as 0.2s. The ratio of volume of reference chamber to that of empty sample

Fig. 2. The cylindrical and crushed & sieved samples with different particle sizes.

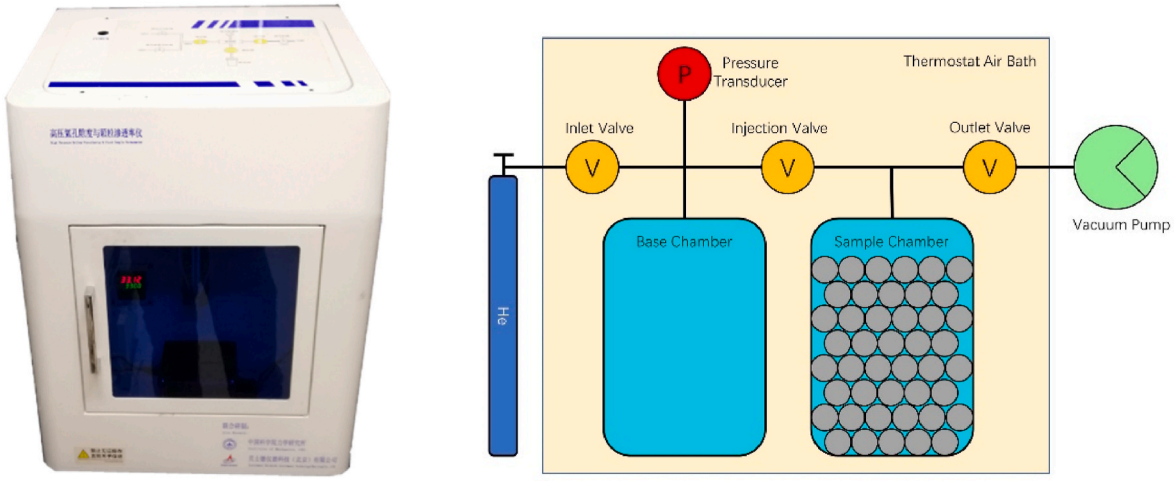

Fig. 3. Matrix permeameter and porosimeter and its schematic diagram.

chamber is about 1.7. Several aluminum blocks can be used to fill the void volume of the sample chamber. The leak rate of the apparatus at the pressure of 14 bar is smaller than 120 Pa/30 min. With the self-developed test control and post-process software, the permeability at a number of pressure points can be automatically tested and recorded as pressure decays.

2.3. Testing procedure

A single test procedure includes the following steps: 1) a number of particles with the known mass and bulk density are loaded into the sample chamber; 2) the reference and sample chambers are vacuumed for 600s after the pressure in the system is below 0.2 bar with the inlet valve closed and the injection and outlet valves opened; 3) close the outlet valve and vacuum pump, record the pressure valve (referred to as P_0) when the variation of pressure in a consecutive 120s is smaller than 180 Pa; 4) close the injection valve and open the inlet valve until the value of the pressure transducer reaches the target value, record the pressure (referred to as P_1) when the variation of pressure in a consecutive 300s is smaller than 180 Pa; 5) open the injection valve, record the elapsed time and pressure with a sampling rate of 0.2s until the variation of pressure is smaller than 180 Pa in a consecutive 1,200s (the final pressure is referred to as P_2) and the test is completed. Fig. 4 depicts the process of the test, and a typical pressure versus time curve of the whole process is shown in Fig. 5. The procedure is similar to that introduced (Cui et al., 2009), with the following improvements: first flushing using experimental gas was replaced with vacuuming the chambers in the stage 2); second, the judgement rules for pressure balancing for all the steps were optimized and specified explicitly.

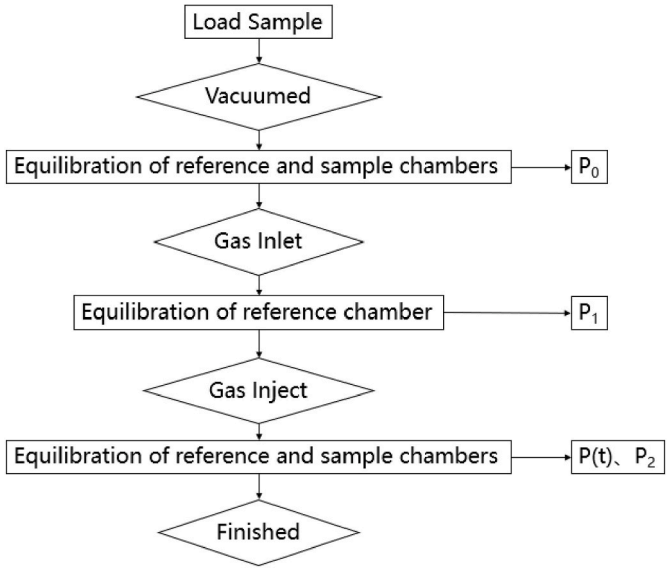

Fig. 4. Flow chart of the test procedure.

2.4. Analysis procedures

2.4.1. Calculation of basic parameters

Pore volume V_P is calculated as

$$V_P = V_b\left(\frac{P_1/Z_1 - P_0/Z_0}{P_2/Z_2 - P_0/Z_0} - 1\right) - (V_s - V_{bulk}) \quad (1)$$

where, Z_i is the helium gas compression factor at the corresponding P_i (i = 1, 2, 3), V_b is the volume of reference chamber, V_s is the volume of the sample chamber before the sample is loaded and does not include the volume of filling blocks when used.

Porosity φ is calculated as

$$\varphi = \frac{V_P}{V_{bulk}} \times 100\% \quad (2)$$

Volume fraction $F_R(t)$ is calculated as

$$F_R(t) = 1 - \frac{(K_c + 1)(\rho_{c0} - \rho(t))}{\rho_{c0} - \rho_0} \quad (3)$$

where $1 - F_R(t)$ denotes the fraction of the amount of gas that enters the particles from the starting point to time t with respect to the final amount of gas that enter the particles when equilibrium has been reached, K_c is the ratio of the volume outside the sample in both the reference chamber and the sample chamber with respect to the pore volume of the sample, ρ_{c0} is the average gas density in the apparatus at the third step in Section 2.3, ρ_0 is the density of gas at P_0, $\rho(t)$ is the gas density at $P(t)$, which is recorded in the fifth step in Section 2.3 and can be calculated according to the equation of state of He. More details about the calculations of other basic parameters can be found in the appendix.

The radius of the particles, R_a , can be preliminarily determined as the average aperture of the screens used, and is listed in Table 2.

2.4.2. Curve fitting method

Assuming the particles are spherical, gas expanding into the pore space of the particle obeys a one-dimensional model in the spherical coordinate system (Cui et al., 2009). The analytical solution of this

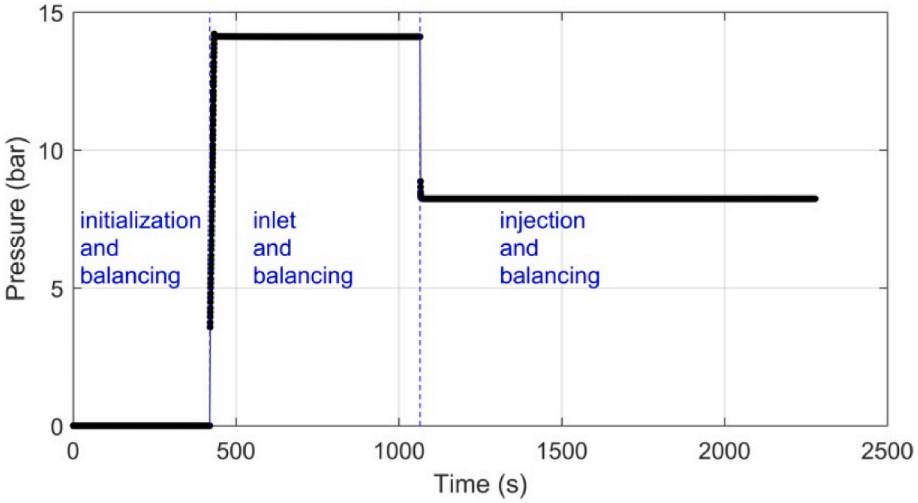

Fig. 5. Variation of pressure with time.

Table 2
Relationship between R_a and the mesh sizes of screens used.

Mesh size	Particle radius (mm)
4–8	1.625
8–12	1.025
12–16	0.625
16–20	0.54

model has the following form,

$$F_R(t) = 6K_c(K_c+1)\sum_{n=1}^{\infty} e^{-\frac{k\alpha_n^2 t}{\mu c_g \varphi R_a^2}} \frac{1}{K_c^2\alpha_n^2 + 9(K_c+1)} \tag{4}$$

where α_n is the n_{th} root the transcendental equation $\tan\alpha = \frac{3\alpha}{3+K_c\alpha^2}$. When $\frac{kt}{\mu c_g \varphi R_a^2} > 0.1$ and K_c is large enough, a linear fit can be calculated for the late stage of the decay curve $\ln(F_R(t))$. The slope s_1 can be determined according to

$$\ln(F_R(t)) = f_0 + s_1 t \tag{5}$$

and the permeability, k, is calculated according to the following relationship,

$$k = -\frac{R_a^2 \varphi \mu c_g s_1}{\alpha_1^2} \tag{6}$$

in which μ is the viscosity of gas, and c_g is the coefficient of compressibility. It is also referred as the late time analysis procedure introduced in Cui et al.'s work (Cui et al., 2009). However, there is no clear definition about the data points that corresponds to late time analysis. The variation of permeability with different range selections is discussed in a latter section. When permeability is fitted, it can be substituted into Eq. (4), and the forward-predicted $F_R(t)$ can be calculated. According to Eq. (3) and the equation of state of He, the forward-predicted $\rho(t)$ and $P(t)$ can also be determined. Besides late time analysis, there is another algorithm called early time analysis that processes data points in the early stage, and is not widely used. However, the early time analysis is not discussed in this work due to the few early-stage data points that were captured in many situations. When referring to curve fitting method in this paper, it applies to late time analysis.

2.4.3. Optimization method

The condition that permeability determined through linear fitting of $\ln(F_R(t))$ at the late stage can represent the whole permeation process is that gas enters the pore space in the crushed particles in accordance with a single permeability value. However, it is not widely satisfied for all samples, and the forward-predicted pressure decay curve based on curve fitting permeability may deviate significantly from the measure one. Therefore, an optimization method is proposed here to determine the permeability that ensures the SSE between the forward-predicted pressure decay curve and the measured one is smallest. The main differences between this method and the curve fitting method include:

1) the starting point that gas enters the pore space of crushed particles is determined based on the porosity and mass of the crushed particles, and the data points after that are used for optimization process.
2) the permeability determined by curve fitting and with the first available data point is set to be the initial lower and upper limit of optimized permeability, and a bisection method is iteratively applied to approach the optimal solution.

A flow chart for this method is shown in Fig. 6. The steps include:

1) the pressure P_3 that gas starts to enter the void space of crushed particles is determined. The density ρ_3 at P_3 is calculated based on mass balance.

$$\rho_3 = \frac{\rho_1 V_b + \rho_0(V_s - V_{bulk})}{V_b + V_s - V_{bulk}} \tag{7}$$

Then, P_3 can be calculated based on the equation of state of He. The starting time t_3 can be determined through the interpolation of pressure decay curve. The time value of all the data points is offset to make t_3 as the zero point, and the first data point whose time is larger than zero is marked as (t_4, P_4).

2) A preliminary curve fitting permeability, k_0, is determined by curve-fitting all the data points after t_4.
3) Another preliminary permeability, k', is calculated using the following relationship.

$$F_R(t_4) = 6K_c(K_c+1)e^{-\frac{k'\alpha_1^2 t_4}{\mu c_g \varphi R_a^2}} \frac{1}{K_c^2\alpha_1^2 + 9(K_c+1)} \tag{8}$$

4) The initial lower limit of permeability, K1, is set to be the smaller one between k_0 and k', while the initial upper limit of permeability, K3, is the larger one. K2 is the average of K1 and K3.

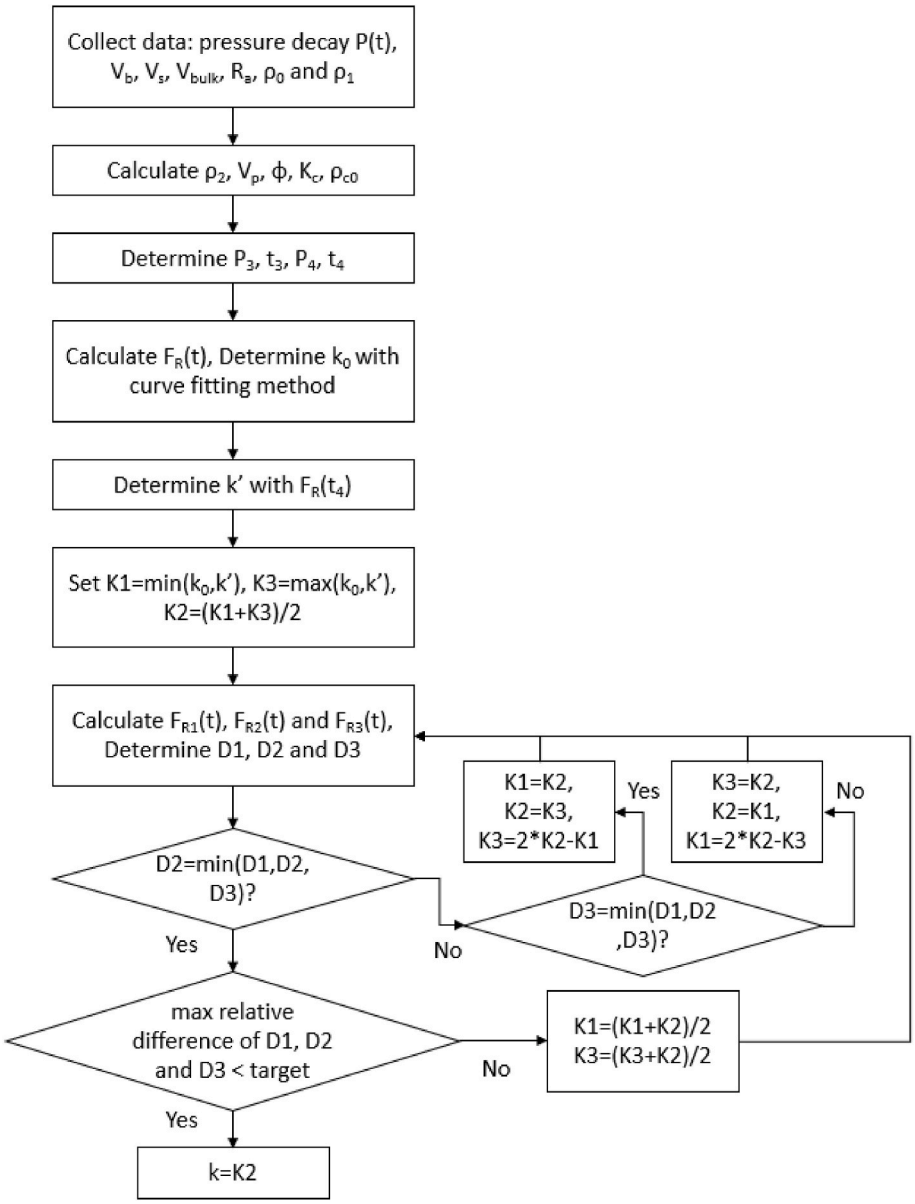

Fig. 6. Flow chart of the optimization process.

5) Substitute K1, K2 and K3 into Eq. (4) to replace k, and calculate the corresponding $F_{R1}(t)$, $F_{R2}(t)$ and $F_{R3}(t)$. The SSE between them and the measure $F_R(t)$ are calculated and referred to as D1, D2 and D3, respectively.

$$D_i = \sum_{n=1}^{m} \left(F_R(n) - F_{Ri}(n)\right)^2, i = 1, 2, 3 \tag{9}$$

where m is the number of data points used.

6) If D2 is the smallest one among D1, D2, D3 and the largest relative difference (the ratio of the absolute difference to the average value) between any two of the three is smaller than the target value (10^{-4}), then K2 is the optimal solution, and the calculation procedure is completed.

7) If D2 is the smallest one among the three, but the largest relative difference is larger than the target value, then K1=(K1+K2)/2, K3=(K3+K2)/2 and go to the fifth step.

8) If D1 is the smallest one among the three, then K3=K2, K2=K1, K1 = 2*K2–K3 and go to the fifth step. if D3 is the smallest one, then K1=K2, K2=K3, K3 = 2*K2–K1, then go to the fifth step.

3. Results and discussion

3.1. Influence of analysis region

Take the crushed 8–12 Mesh BS22-45JX sample as an example to investigate the effect. Due to the small sampling interval adopted, the high-precision thermostat air bath, and etc., the record pressure is declining continuously without large fluctuations (Fig. 7a). P_3 is determined to be 3.003 bar, and the pressure after 100s rises and falls in the range of a resolution, 60Pa. The corresponding $Ln(F_R(t))$ is plotted in Fig. 7b. It can be seen that $Ln(F_R(t))$ declines fast initially, then declines linearly, finally swings between −4 and −33 which is limited by the resolution of the pressure transducer. These three stage decline characteristic is similar to that obtained in Achang et al.,'s work (Achang et al., 2017). Interestingly, this is the same type of decline curve that shale oil and gas wells have, although that appears to have to do with

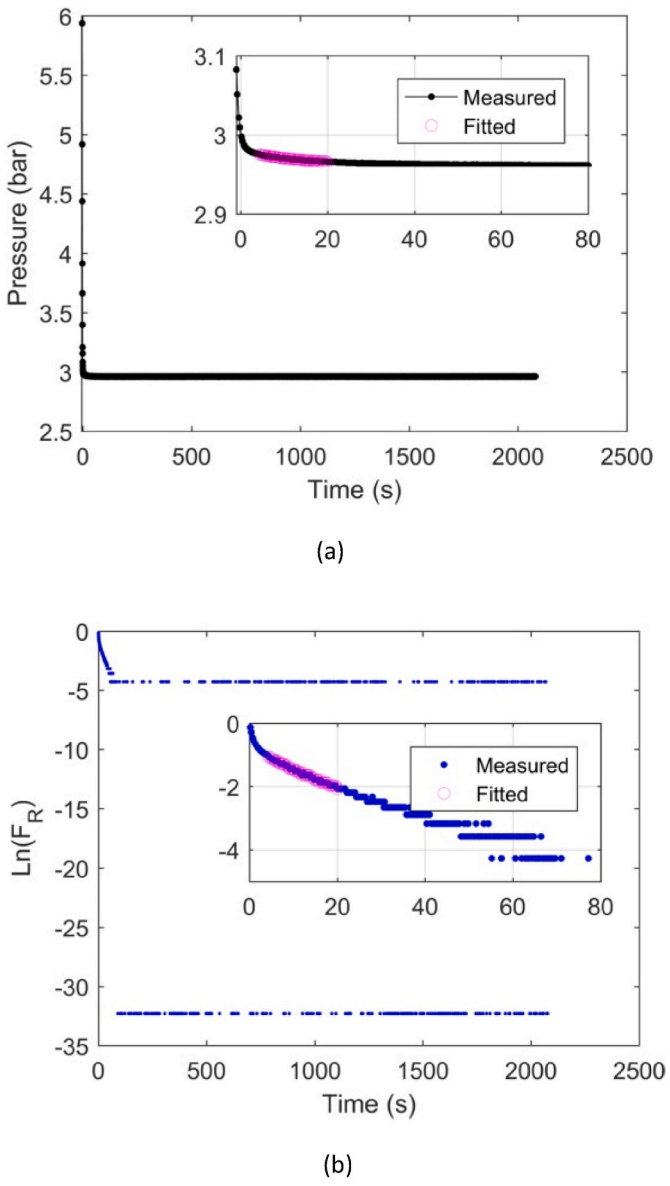

Fig. 7. The decay curves for pressure and $F_R(t)$ of the 8–12 Mesh BS22-45JX sample.

much more than what controls the curve in a crushed shale sample cell.

At the early stage, there is no strong linear relationship between $Ln(F_R(t))$ and t. A linear relationship only exists in the middle stage. However, there is ambiguity in the visual picking starting and end points of the linear section. A scheme is proposed to evaluate the linear segment. Firstly, the end point is selected that the difference between its pressure P_{end} and the final equilibrium pressure P_2 is n times the resolution of the pressure transducer P_{res}, as follows:

$$n = \frac{(P_{end} - P_2)}{P_{res}}, n = 1, 2, 3, \cdots, 10 \tag{10}$$

Then for every end-point selection, the starting point moves from the first data point to the right and makes sure there are at least a certain number of data points that define the linear segment. Line segments with too few points might achieve a better goodness of fit than longer line segments. However, they are not adequately representative and should be excluded. For high-permeable samples, the number of valid data points is limited. Considering the balance of these two above aspects, the minimal number of data points of a linear segment is set to 6. A Linear fit of Eq. (5) with the data points between the starting and end points is calculated, and the goodness of fit, R^2, determined. For every end-point selection, the best-fit permeability is determined where the corresponding R^2 is greatest. Table 3 lists the greatest R^2, best-fit permeability, indexes of starting and end data point for every end-point selection. It can be found that R^2 and permeability vary with different starting and end points. When the end point approaches the swing area near the equilibration, the permeability is small. When the starting point moves forward to a certain position, the fitted R^2 increases significantly. There is a middle section where the fitted R^2 is highest (the adopted data points are denoted with purple circle in Fig. 7), and the fitted permeability vary in the range of 10%. With the above procedure, the ambiguity caused by the different selections of data points can be reduced.

3.2. Comparison of bulk permeability determined by optimization and curve fitting methods

Then optimization method is performed on the entire pressure decay curve to determine a single equivalent permeability. Limited by the resolution of pressure transducer, the pressure value will rise and fall in a resolution over a certain period of time at the late pseudo-steady stage (Achang et al., 2017) when the decline of pressure is nearly completed. For the optimization method, if all the data points are used, the contribution of pseudo-steady stage to the SSE will undoubtedly increases. The late stage will be over weighted and an underestimated permeability will be calculated. Therefore, the data points used needs to be screened before optimization. The screening rule is defined as follows: as the pressure declines, only the first data points that each pressure appears are kept. In addition, minimum pressure of the used data point should be at least one resolution (60Pa) larger than the final equilibration pressure P_2 to eliminate the influence of tail swing. The optimal equivalent permeability is determined as 35.8 nD for this sample, which is obvious larger than that determined by curve fitting.

Once permeability is determined, the pressure decay curve can be forward-predicted based on Eq. (4) and Eq. (3). The consistency between predicted and measure curve can be used as a criterion to evaluate the applicability of a method to determine bulk permeability. The results of using these two methods are plotted in Fig. 8. It can be seen that, for the discussed 8–12 Mesh BS22-45JX sample, the slopes of measured and forward-predicted curves $Ln(F_R)$ with non-dimensional time $\tau = \frac{k\alpha_n^2 t}{\mu c_g \varphi R_a^2}$ are close only when τ is larger than 0.1. Overall, the decline of pressure predicted by the curve-fitting method is slower than the measured decline.

Although there are still observable deviations between prediction and measured curves, the pressure decay curve predicted by the optimization method is more consistent than that predicted by the curve fitting method (Fig. 8), and is more close to the true bulk permeability. Moreover, the effect of deviation of optimal prediction at the late-time stage is visually aggravated in the Ln (F_R) versus non-dimensional time plot. The deviation looks stronger than the actual one in a semi-logarithmic plot when Ln (FR) is smaller than −2. **About 77% of pore space has been filled with He when Ln(F_R) is -1.5, the latter**

Table 3
The best-fit results for different end-point selections.

n	Adjusted R^2	Fitted Permeability (nD)	Starting Point Index	End Point Index
1	0.176	2.4	2	562
2	0.963	13.9	6	216
3	0.979	14.5	11	177
4	0.984	15.2	15	134
5	0.986	15.7	15	120
6	0.989	16.5	15	101
7	0.990	17.0	15	92
8	0.990	17.3	15	79
9	0.989	17.6	15	72
10	0.989	18.1	15	65

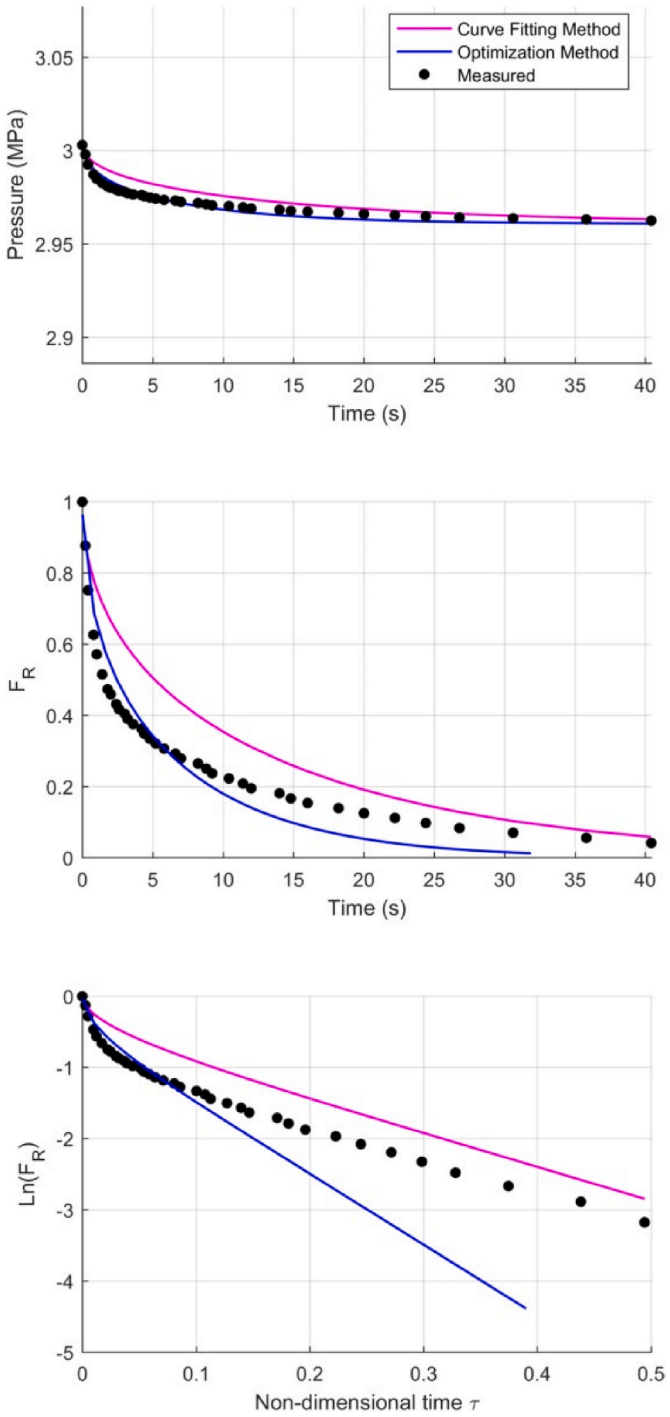

Fig. 8. The pressure decline curves of the 8–12 Mesh BS22-45JX sample.

segment only represents less than 1/4 of the entire pore space. Since the optimal predicted curve cannot perfectly match the measure one, it can be inferred that the studied sample has at least two stage of pore space. In order to match the measured data more accurately, a dual-porosity model needs to be proposed which is the direction of the future research. Although the two-stage feature has been recognized, whether the early-time fast decline is caused by larger natural pores or sample damage cannot be determined only with this single comparison.

Another sample, 12–16 Mesh RS4-35JX, is taken for comparison. The curve fitting permeability (98.8nD) is closer to the optimal permeability (118.5nD), comparing with the BS22-45JX sample. The pressure decay curve forward predicted by curve fitting method is closer to the measure one, comparing with 8–12 Mesh BS22-45JX sample (Fig. 9). In other words, the model that assumes gas enters to particles with a single determined permeability and derives the analytical solution (Eq. (4)) can characterize this sample well. Both the predicted and measured Ln (F_R) versus non-dimensional time curves of this sample show an early-time fast-decline stage and a late-time exponential decay stage. The early-time acceleration is mainly due to that the effect of 2nd and latter items in the cumulative item at the right hand side of Eq. (4) cannot be neglected when time value is very small, not the existence of larger natural or sample-damage-induced pores.

From these two samples, it can be found that when the pressure decay curve can be fit by Eq. (4), such as the 12–16 Mesh RS4-35JX

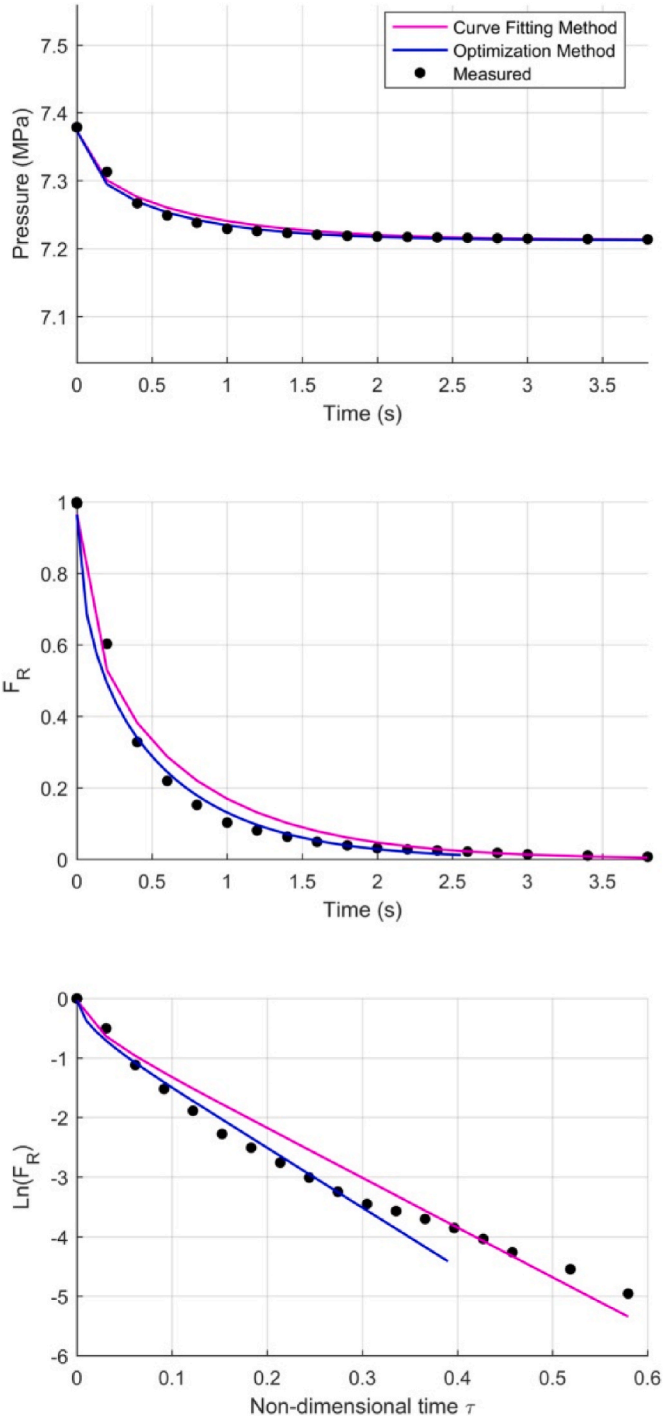

Fig. 9. The pressure decline curves of the 12–16 Mesh RS4-35JX sample.

sample, the curve fitting method is able to represent the whole stage, and is close to the bulk permeability. On the other side, such as the 8–12 Mesh BS22-45JX sample, the permeability obtained with curve fitting method is closer to a lower value that relates to the late stage, and will be obviously smaller than the optimal value that corresponds to the whole process and is more close to the bulk permeability.

3.3. Repeatability of tests

The crushed 12–16 Mesh BS22-45JX sample has been tested twice independently. Table 4 lists the porosity and permeability determined by curve fitting and optimization. The porosity values are close, while the repeatability of optimization method is better than that of curve fitting method. The decay curves of pressure and F_R are plotted in Fig. 10. Pressure does not decline continuously at the later stage, which indicates a good gas tightness of the apparatus. This avoids the difficulty of distinguishing whether gas enters particles or leaks from the chamber as both two phenomena show the characteristics of pressure decline. In addition, the small-amplitude fluctuation of pressure is consistent with the temperature fluctuation at the late stage, and no obvious pressure rise is observed in the tests. As the equilibrium pressure P_1 at the gas inlet step of these two tests cannot be controlled to the same very precisely, the final equilibrium pressure P_2 might varies accordingly. However, the relationships between F_R and non-dimensional time τ of these two tests are very consistent. A sample that is close to BS22-45JX in the same well is tested five times consecutively, and the repeatability is further verified. More details will be found in the appendix. This good repeatability lays a good foundation for the following discussion.

3.4. Variation of permeability with pressure

Gas flow at the nanometer scale obeys multiple non-Darcy flow regimes, such as Knudsen diffusion, slippage, etc. (Fathi et al., 2012; Javadpour, 2009; Jiang et al., 2017). The determined permeability at a certain pressure is actually the "apparent" permeability that varies with pressure. For the crushed BS22-45JX and RS4-35JX samples with different particle sizes, tests with final equilibrium pressures around 3, 5, and 7 bars are performed and the apparent permeability are determined with the above two methods, the results are shown in Figs. 11 and 12, respectively.

For same particle size, the crushed apparent permeability k declines as pressure P increases. A sample that is close to BS22-45JX in the same well was tested at smaller pressure intervals between 3 and 12 bar, and the same linear relationship was verified. More details are given in the appendix. This trend is similar with the results of existing researches that can be described using the Klinkenberg equation (Dadmohammadi et al., 2016; Fathi et al., 2012; Firouzi et al., 2014; Hoang et al., 2017; Javadpour, 2009; Jiang et al., 2017; Li and Sultan, 2017; Profice et al., 2012). The following equation is used to fit the data points of permeability versus pressure within the range of 3–12 bars.

$$k_{app}(P) = k_{3bar}\left(1+\frac{b}{P}\right) \Big/ \left(1+\frac{b}{3}\right) \tag{11}$$

where P is the equilibrium pressure with the unit of bar, k_{3bar} is the apparent permeability at 3 bar with the unit of nD, b is a coefficient that is positively related to the rate of permeability decreasing with pressure. The ratio of apparent permeability at pressure P with respect to that at 3 bar is defined as:

$$\lambda_k(P) = \frac{k_{app}(P)}{k_{3bar}} = \left(1+\frac{b}{P}\right) \Big/ \left(1+\frac{b}{3}\right)$$

The fitted results for BS22-45JX and RS4-35JX with different particle sizes are listed in Table 5 and Table 6, respectively. Within the test pressure range, there is a strong positive linear relationship between permeability obtained by the optimization method and the coefficient of compressibility, C_g which is close to $\frac{1}{p}$. This correlation is stronger than that of the curve fitting permeability and C_g, especially for the RS5-45JX samples with different particle sizes.

Table 4
Permeability determined from two tests of 12–16 Mesh BS22-45JX sample.

	Porosity (%)	Curve Fitting Permeability (nD)	Optimal Permeability (nD)
1st	4.10	12.4	35.8
2nd	4.12	17.5	36.4

3.5. Variation of permeability with particle size

The particle size of the sample decreases as the mesh size of sieves increases. From Figs. 13 and 14, it can be observed that apparent permeability of samples with different particle sizes varies. For the BS22-45JX sample, the apparent permeability at 3 bars decline initially and then varies within a narrow range as the particle size decreases. The trends obtained by the optimization and curve fitting method are consistent, but the curve fitting ones are smaller as the effect of early-time hyperbolic decay segment is not included. For the RS5-45JX sample, the trends obtained by these two methods are different. The optimal permeability at 3 bar decreases continuously as particle size decreases, while the curve fitting permeability varies within a narrow range as the particle size decreases. The irregular changes of curve fitting results might be due to that the period of test time for this relatively high permeable sample is short and only a limited number of data points can be collected. The uncertainty of curve fitting result increases without enough number data points. The elapsed time of test becomes shorter as the particle size decreases and this phenomenon becomes more significant. The characteristics found in this work are more diverse than existing studies that have shown crushed sample permeability increases with particle size (Cui et al., 2009; Peng and Loucks, 2016; Tinni et al., 2013).

Explanations for the variation of permeability with particle size mainly includes three aspects (Achang et al., 2017; Peng and Loucks, 2016; Tinni et al., 2013): 1) system errors of measurement. 2) the test time for small particles is too short with a limited number of useful data, and curve fitting method only focuses on the late stage, not including the early stage. 3) Artificial and natural fractures are more frequently present in large particles. In this study, with the testing apparatus and procedures with good repeatability, the effect of the first aspect is reduced. With the optimization method, data points are fully utilized to overcome the shortage of curve fitting method. The evaluation of the possibility of sample damage during crushing is the focus. In general, scanning electron microscopy (SEM) images is used to reveal the generation of secondary microfractures. However, there always exists a problem of representativeness using this approach. For the BS22-45JX sample, the possibility that artificial secondary microfractures exist only in the 4–8 Mesh sample and disappear with further crushing is small. It is also very difficult to identify this sudden change with particle size with SEM images convincingly due to resolution. Therefore, a new method needs to be proposed to judge the generation of large pore structure like microfractures during crushing.

Based on the existing research on nanometer pore-scale shale gas flow, the gas flow capability will increase at the lower pressure due to Knudsen diffusion, slippage and etc. The strength of these effects relates to Knudsen number which is a function of not only pressure, also pore width. Therefore, when the pore structure at the micrometer to nanometer scale changes significantly, beside absolute permeability, the variation of apparent permeability with pressure (referred to as non-Darcy feature) will change correspondingly (Achang et al., 2017; Cui et al., 2009; Jiang et al., 2017; Mehmani et al., 2013). For example, if there are microfractures in large particles, but no microfractures in

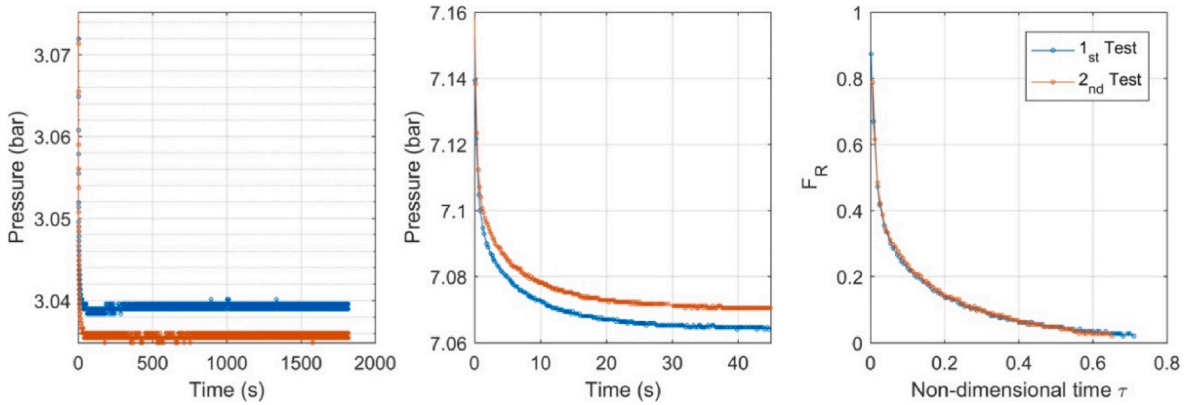

Fig. 10. Repeatability of test of 12–16 Mesh BS22-45JX sample.

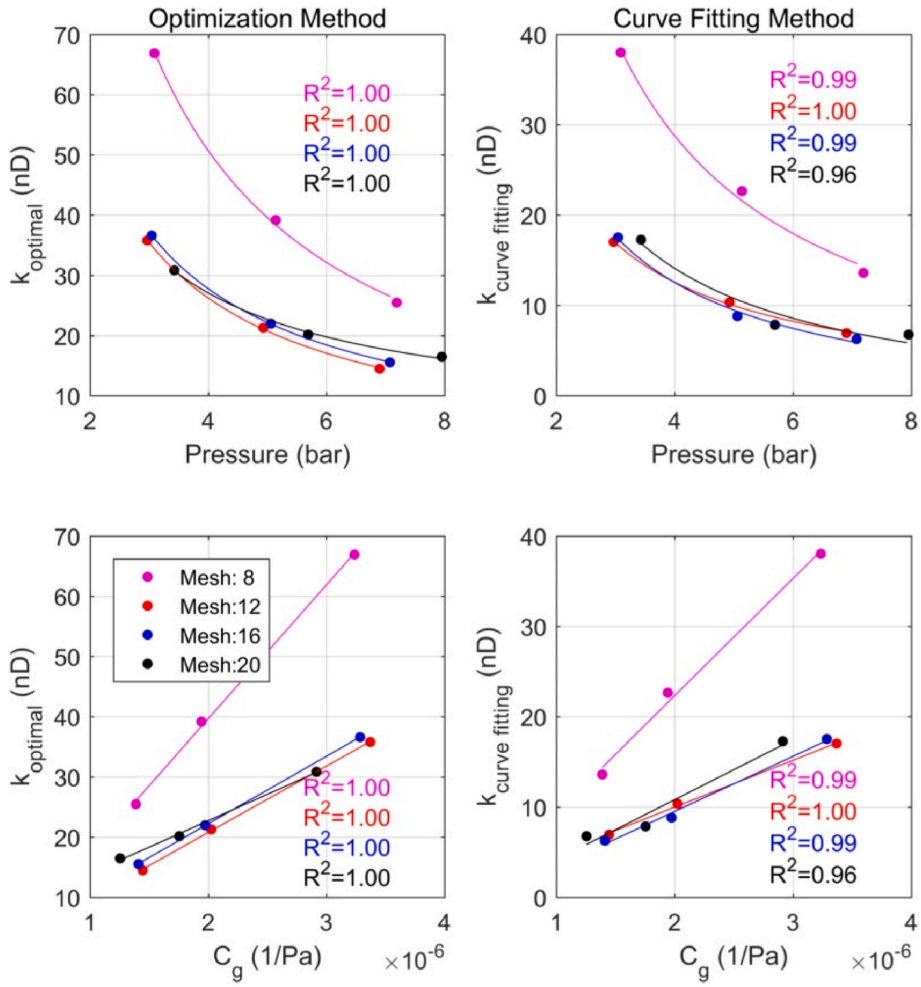

Fig. 11. Variations of apparent permeability with P, C_g for BS22-45JX samples.

smaller particles, the non-Darcy feature of these two particles will also be different as the Knudsen diffusion and slippage effect will decrease with the average throat radius increases. The ratios of apparent permeability at 5, 7 bar with respect to that at 3 bar, $\lambda_{k,5bar}$ and $\lambda_{k,7bar}$, are defined to represent the degree of non-Darcy feature. The variation of these indicators can reflect the change of pore structure during crushing from another perspective.

As shown in Fig. 13 for the BS22-45JX sample, the non-Darcy degrees of the 4–8, 8–12 and 12–16 Mesh samples are basically consistent, while those of the 16–20 Mesh sample is slightly different. It indicates that pore structure has not changed significantly during crushing. Considering the fact that the pore structure has not changed with particle size, the permeability k should be consistent among samples with different particle sizes. However, the apparent permeability at 3 bar of the 4–8 Mesh particles is significantly larger than that of the particles with other particle sizes. Further comparing the optimal-permeability-based forward-predicted $F_R(\tau)$ of samples with different particle sizes at the same equilibration pressure (Fig. 15), the curves overlap. In a non-dimensionless sense, the attenuation processes of samples with different particle sizes are close, which is in agreement with the non-

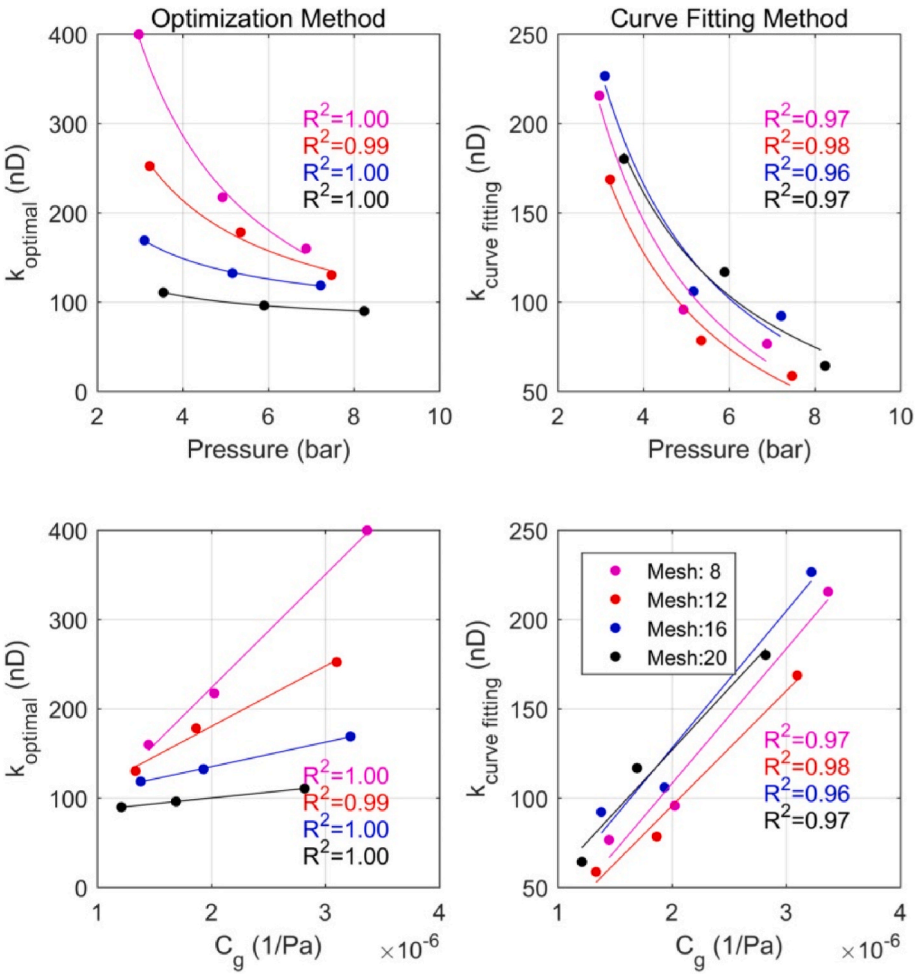

Fig. 12. Variations of apparent permeability with P, C_g for RS4-35JX samples.

Table 5
Fitted parameters of permeability versus pressure for BS22-45JX samples.

	Optimization Method			Curve Fitting Method		
	k_{3bar} (nD)	$\lambda_{k,5bar}$	$\lambda_{k,7bar}$	k_{3bar} (nD)	$\lambda_{k,5bar}$	$\lambda_{k,7bar}$
4-8 Mesh	69.21	0.57	0.39	39.57	0.56	0.38
Mod. 4–8 Mesh	36.27	0.57	0.39	17.26	0.56	0.38
8-12 Mesh	35.42	0.59	0.41	16.89	0.59	0.41
12-16 Mesh	37.12	0.60	0.42	17.63	0.54	0.34
16-20 Mesh	34.39	0.66	0.51	19.64	0.55	0.36

Table 6
Fitted parameters of permeability versus pressure for RS4-35JX samples.

	Optimization Method			Curve Fitting Method		
	k_{3bar} (nD)	$\lambda_{k,5bar}$	$\lambda_{k,7bar}$	k_{3bar} (nD)	$\lambda_{k,5bar}$	$\lambda_{k,7bar}$
4-8 Mesh	392.20	0.57	0.38	208.37	0.52	0.31
Mod. 4–8 Mesh	205.54	0.57	0.38	90.88	0.52	0.31
8-12 Mesh	270.22	0.67	0.52	181.07	0.53	0.32
12-16 Mesh	171.56	0.79	0.69	229.94	0.55	0.36
16-20 Mesh	117.34	0.85	0.79	218.75	0.58	0.40

Darcy feature analysis. Therefore, the conversion coefficient from physical time t to the non-dimensional time τ should be accurate. From the definition of non-dimensional time $\tau = \frac{k\alpha_n^2 t}{\mu c_g \varphi R_a^2}$, the coefficients μ, c_g, φ, α_n are determined only by the equilibrium pressure P_2. The ratio $\frac{k}{R_a^2}$ itself should be fixed, and incorrect determination of the radius value R_a might lead to the deviation of the determined permeability from the actual value.

The radius R_a of the particles is preliminary determined as the average aperture of the screens used. Actually, the shape of the crushed particle is different from the ideal spheres assumed by the model. When the particle is large, the possibility becomes large that two of the three dimensions of the sample match the apertures of screens while the other dimension is smaller than the apertures, and the actual effective radius should be smaller than that determined by the average aperture. For the BS22-45JX sample, the permeability of 8–12, 12–16 and 16–20 Mesh particles are close, and can be considered as more accurate than that of 4–8 Mesh particles. Take the average permeability of 8–12 Mesh and 12–16 Mesh particle as the actual value, the radius of 4–8 Mesh particles can be modified from 1.625 mm to 1.176 mm. The corrected permeability at 3 bar, $\lambda_{k,5bar}$ and $\lambda_{k,7bar}$ are also plotted in Fig. 13 with the mesh size labelled as "Mod. 4–8". The variation of these parameters with particle size for the BS22-45JX sample obtained by the optimization method and curve fitting method are consistent on the overall trend, despite there exist discrepancies on the magnitudes that is due to the limitation of late-time curve fitting as mentioned above.

Considering the possibility of sample damage effect during crushing for the BS22-45JX sample is small, the relatively higher-permeability early stage of the pressure decay curve is mainly caused by the natural large pore structure.

The same correction for the radius of the 4–8 Mesh samples should also be applied on the RS4-35JX sample, and the corrected permeabilities at 3 bar, $\lambda_{k,5bar}$ and $\lambda_{k,7bar}$ are also plotted in Fig. 14 with the mesh size labelled as "Mod. 4–8". For this sample with the optimization

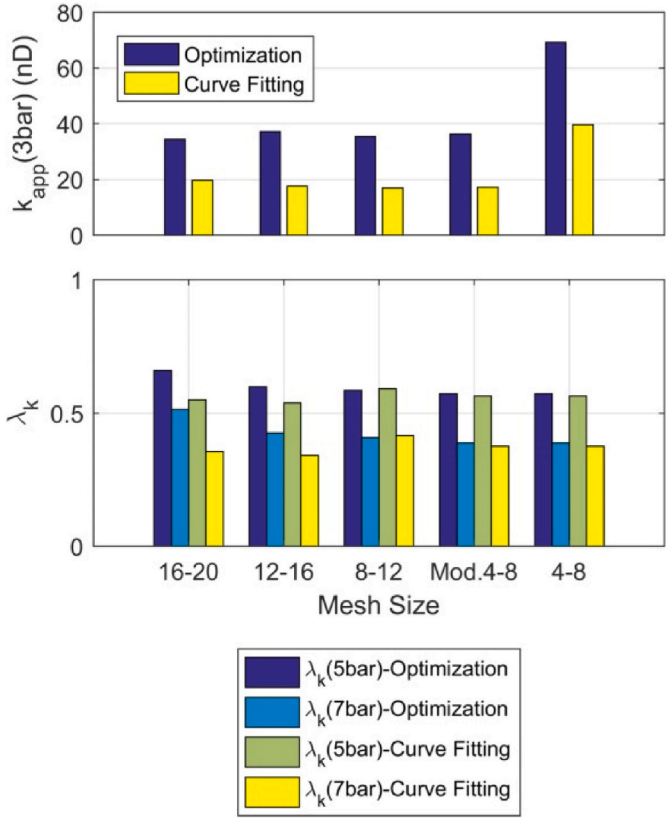

Fig. 13. Variation of permeability and λ_k with pressure in sample BS22-45JX.

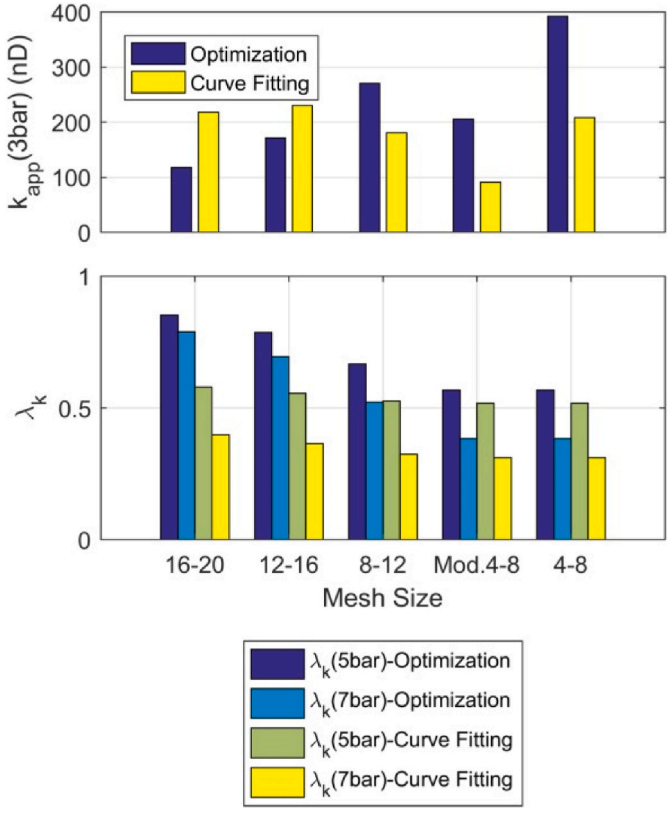

Fig. 14. Variation of permeability and λ_k with pressure in sample RS4-35JX.

method, both the $\lambda_{k,5bar}$ and $\lambda_{k,7bar}$ increase as the particles size decreases, indicating that non-Darcy degree becomes weaker and the pore structure has been obviously modified during crushing. Correspondingly, after correction, the permeability firstly increases then decreases as the particle size decreases. Comparing the optimal-permeability-based forward-predicted $F_R(\tau)$ of samples with different particle sizes at the same equilibration pressure (Fig. 16), the curves are close, but the consistency between different particle sizes is weaker than that for the BS22-45JX sample.

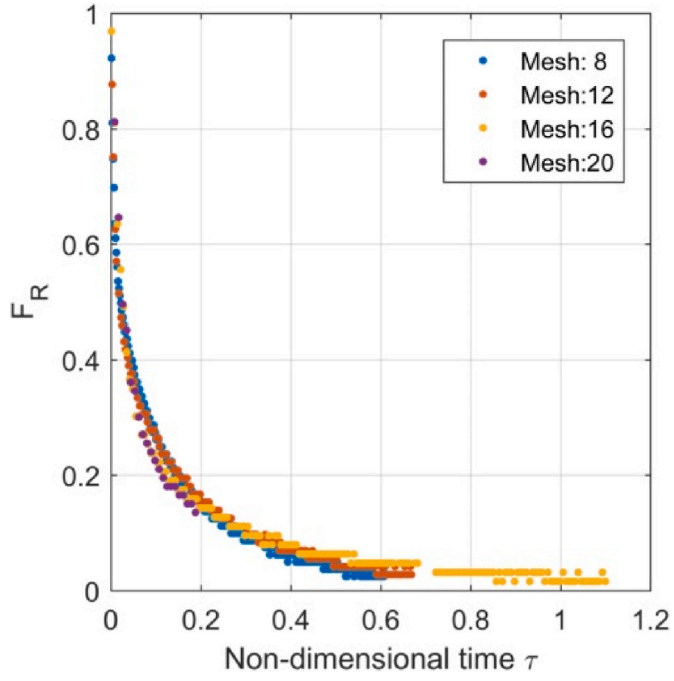

Fig. 15. Decay curve of F_R at 3 bars for BS22-45JX with different particle size.

Table 7 lists the porosity of samples with different particle sizes for RS4-35JX. As particle size decreases, the porosity firstly increases then decreases. This trend is generally consistent with that of permeability with particle size. The turning particle size of permeability is larger and

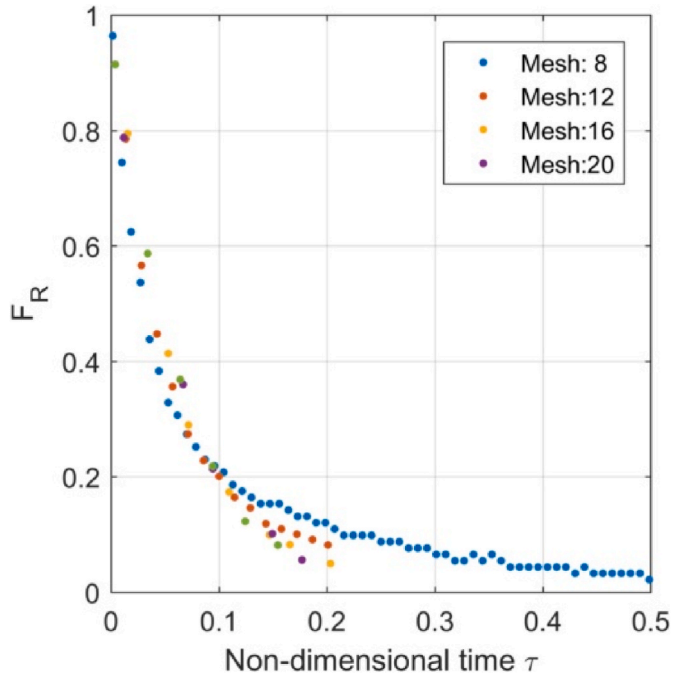

Fig. 16. Decay curve of F_R at 3 bars for RS4-35JX with different particle sizes.

Table 7
Porosity of samples with different particle sizes.

Mesh Size	Porosity (%)
4–8	5.17
8–12	5.32
12–16	5.35
16–20	4.89

it might be due to that permeability is more sensitive to the change of pore structure than porosity. The possible mechanism might be that as the particle size decreases during crushing, firstly, originally-isolated pores are exposed and connected, and the porosity and permeability increases. Further decreasing the particle size, destruction of relatively large pores and microfractures dominates, particles with higher porosity is easier to be screened out due to their small grain volume and the porosity and permeability become smaller. Fig. 17 schematically shows this change with an idealized pore system of the shale gas reservoir that is constructed under the guidance of existing literatures (Loucks and Reed, 2014; Wu et al., 2020b). More developed pore system with a better connectivity is observed in the pyrobitumen than kerogen and mineral, and plays an important role in the storage and flow of shale gas.

Different from the BS22-45JX sample, the measured pressure decay curves of the RS4-35JX sample with different particle sizes all can be fitted well with the optimization permeability and a unipore homogeneous model represented by Eq. (4). However, the permeability and non-Darcy degrees of samples with different particle size varies obviously. Although this sample does not show obvious two-stage or dual porosity feature, its pore structure change significantly with gradual crushing.

Combining the analysis of the above two samples, the optimization analysis of pressure decay curves of samples with different particles size allows for a more comprehensive understanding on crushed sample structure. Whether the sample has significant two-stage pore structure features can be identified, and whether the two-stage features are natural or secondary can also be identified.

The continuously decrease of non-Darcy (induced by Knudsen diffusion, slippage and etc.) degree with the decrease of particle size can further reflects more details on the change of the pore structure. It is assumed that patches of matrix with different permeability are in series along the gas flow direction, and the permeability of the whole matrix should be the harmonic-mean permeability of matrix patches with different properties. It can be easily derived that the non-Darcy degree of the whole sample is between the non-Darcy degrees of different matrixes. Based on this, it can be inferred that for the RS4-35JX sample, as the particle size decreases, the proportion of pore throats with small radius and strong non-Darcy features decreases and the distribution of pore throat radius gradually narrows, leading to a continuous decrease of non-Darcy degree. It should be mentioned that this phenomenon cannot be disclosed by the curve fitting method that is only for the late stage.

From the above analysis, there are three main aspects that may lead to variations of permeability with particle size. One is the deviation between the radius determined as the average aperture of the screens used and the actual radius of the particles, and this effect is more obvious when the particles are relatively large. The second one is that the pore structure changes significantly during crushing. As the particle size decreases, isolated pores might be connected, and large pores might be destroyed, leading to variations of permeability. The third one is the

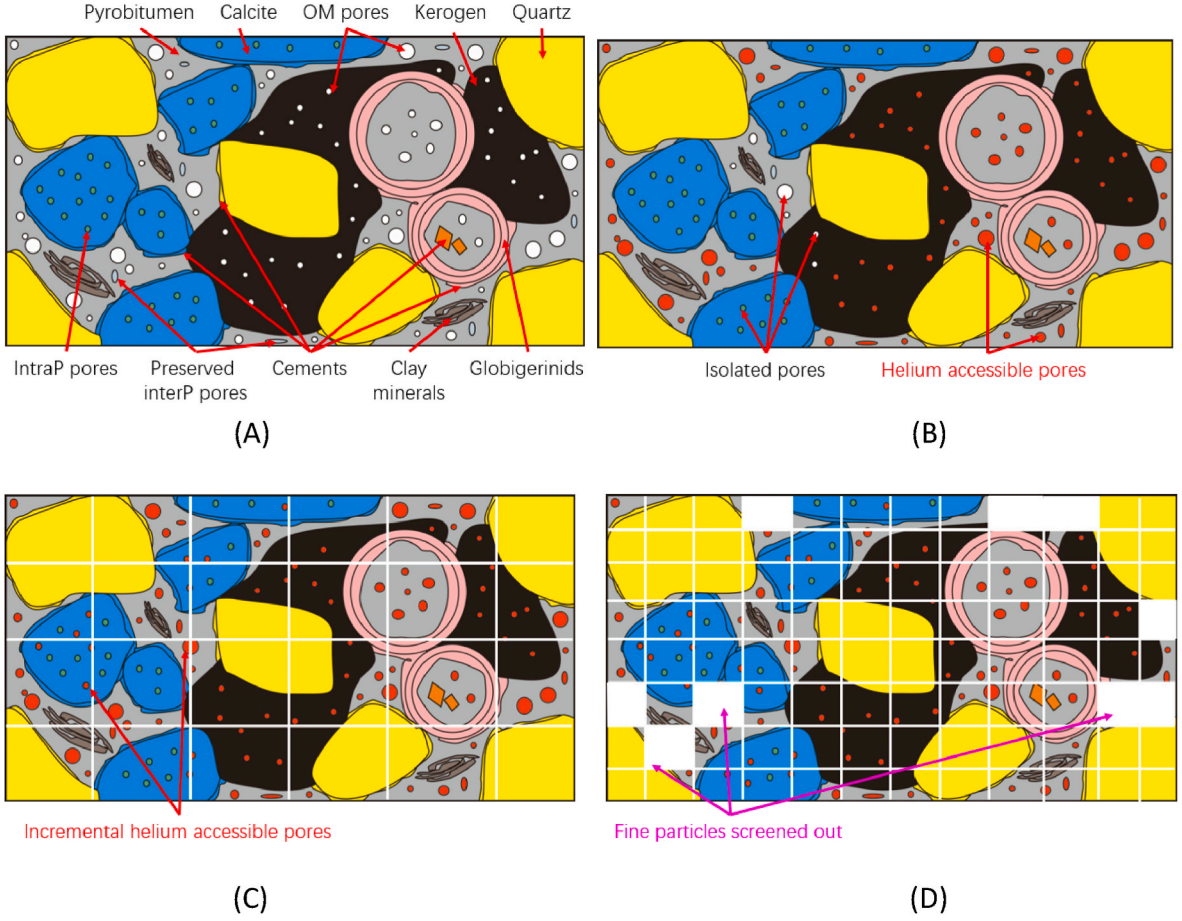

Fig. 17. Schematic of porosity change of particles during crushing. (A) Idealized pore system of shale. (B) Original pore connectivity. (C) Porosity increase after primary crushing. (D) Porosity decrease due to fine particles screened out.

particles are so small that the available pore space fills too rapidly to derive a quality test result. When conditions permit, it is necessary to select a sample whose non-Darcy degree does not vary with particle size to correct the possible deviation of particle radius when different types of screens or crusher are used. Measuring the variation of permeability with pressure and particle size can also be helpful to further understand the characteristics of pore structure.

Based on the above discussion, further investigation can be performed to improve the understanding of matrix flow characteristics and its application in engineering, includes: 1) For samples with obvious two-stage characteristics, it is necessary to propose a dual-porosity model and optimized solving procedure to better match the whole process of pressure decay. Existing approaches prefer to fit these two stage separately and the transition stage is not well resolved. 2) There exists a certain amount of primary water in shale reservoir. Pilotage work has been performed to discuss the recovery of water-bearing conditions and the influence of moisture on the permeability of crushed shale (Achang et al., 2019). The differences in pressure decay characteristics between moisture and dry samples with different pore structures at different pressures need to be further revealed. 3) Currently, the crushed permeability is able to reflect the relative level of matrix permeability and is used as an indicator to select the sweet segment along the vertical direction. In order to further apply directly in the history matching of production dynamics, the influence of effective pressure on the matrix permeability should be clarified and a comprehensive understanding on the connection between crushed and plug sample is needed.

4. Conclusion

In this study, an optimization method for determining the equivalent bulk permeability of crushed shale samples ensures that the sum of errors between the measured and forward predicted pressure decay curves is smallest is developed. The optimization method shows a better repeatability and more obvious regularities on the change of apparent permeability with pressure and particle size, and is more appropriate to present the bulk characteristic comparing with late-time curve fitting method. A linear relationship between apparent permeability and coefficient of compressibility is found between 3 and 12 bar for the studied shale samples from Ordovician Wufeng Formation in Sichuan basin, China. Discrepancy between crushed samples with different particle size on the change of apparent permeability with pressure (non-Darcy feature) is proposed as a criterion of whether pore structure has changed significantly. For large particles, the particle size determined based on the mesh size of screens used may be overestimated. Variation of permeability with particle size might be nonmonotonic, depending on the change feature of pore structure during crushing. The distinctive characteristics on the multiple-stage decline and crushing-induced pore structure change aspects between the two studied samples suggest the diversity of natural shale reservoir matrix. The optimization analysis of pressure decay curves of samples at multiple equilibration pressure with different particles size provides a viable approach of identification. These finding lay a foundation for a further finer characterization of matrix permeability, and can be helpful for petroleum engineering field to gain a deeper understanding the influence factors of crushed permeabilities.

Declaration of competing interest

The authors declare that they have no known competing financial interests or personal relationships that could have appeared to influence the work reported in this paper

Data availability

The data that has been used is confidential.

Acknowledgements

This work is supported by the Strategic Priority Research Program of the Chinese Academy of Sciences (Grant No. XDA14010304), the National Natural Science Foundation of China (Grant No. 42030808, 41690132 and 41872163) and the PetroChina Science and Technology Major Project (2019F-31-01).

Appendix

1 Mineral Composition of the Studied Samples

The samples are analyzed at Keyuan Engineering Testing Center, Sichuan, China with a Panalytical X'Pert PRO MPD X-ray diffractometer. The detail of preprocess and test procedure can be found in the literature (Jiang et al., 2022). The main mineral compositions of these two samples are quartz, feldspar and carbonate.

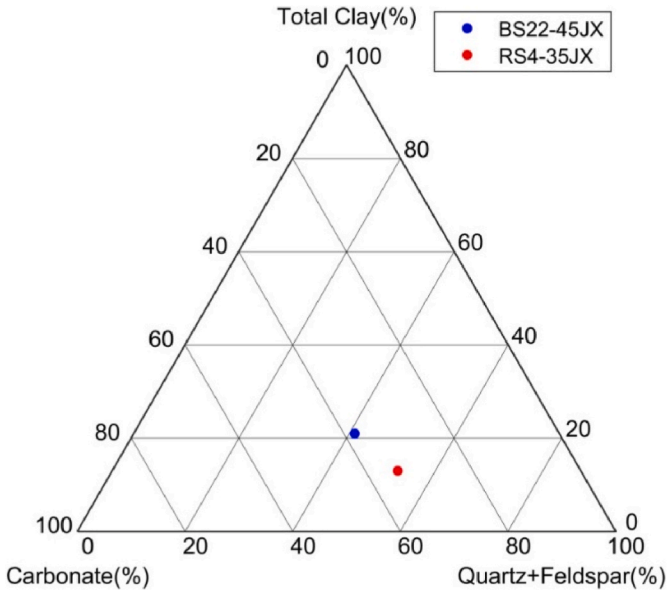

Fig. A1. Ternary diagram of the XRD mineral composition for the study shale samples.

2 Large area mosaic SEM imaging

The samples were imaged with a Zeiss Merlin FE-SEM at Core Labs, Institute of Geology and Geophysics. The highest resolution is 4 nm and the size of the imagine area is about 400μm × 400 μm. The detail of preprocess and test procedure can be found in the literature (Wu et al., 2020a). It can be observed from the large area mosaic SEM images that Organic pores are the most developed and contribute mainly to the pore space.

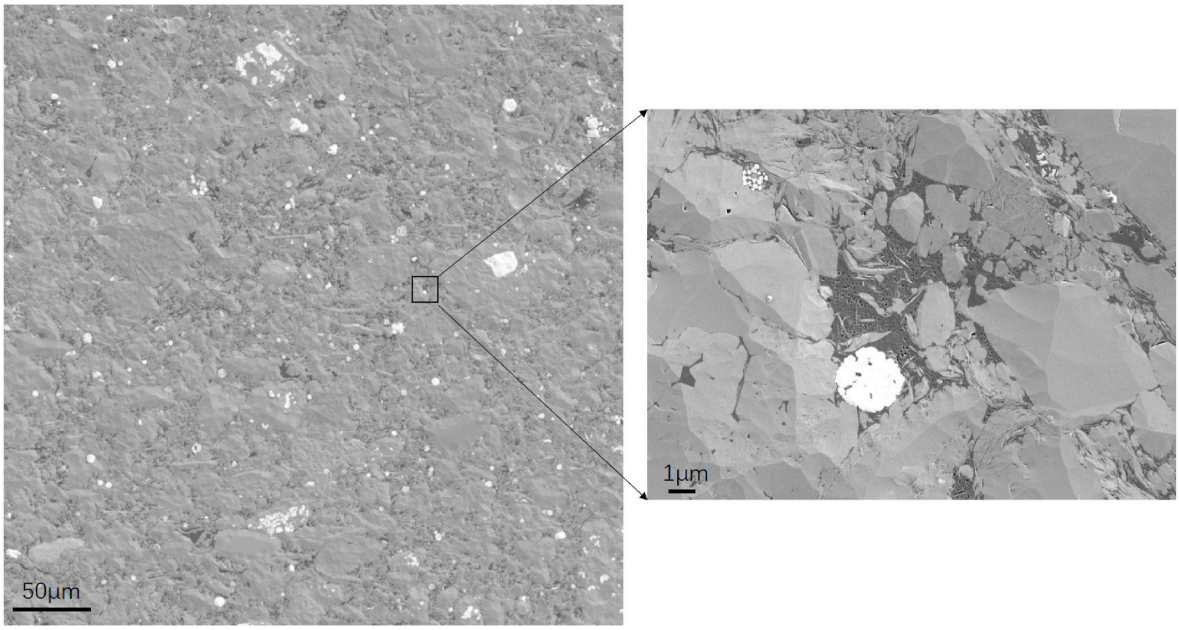

Fig. A2. Large area mosaic SEM imaging of BS22-45JX.

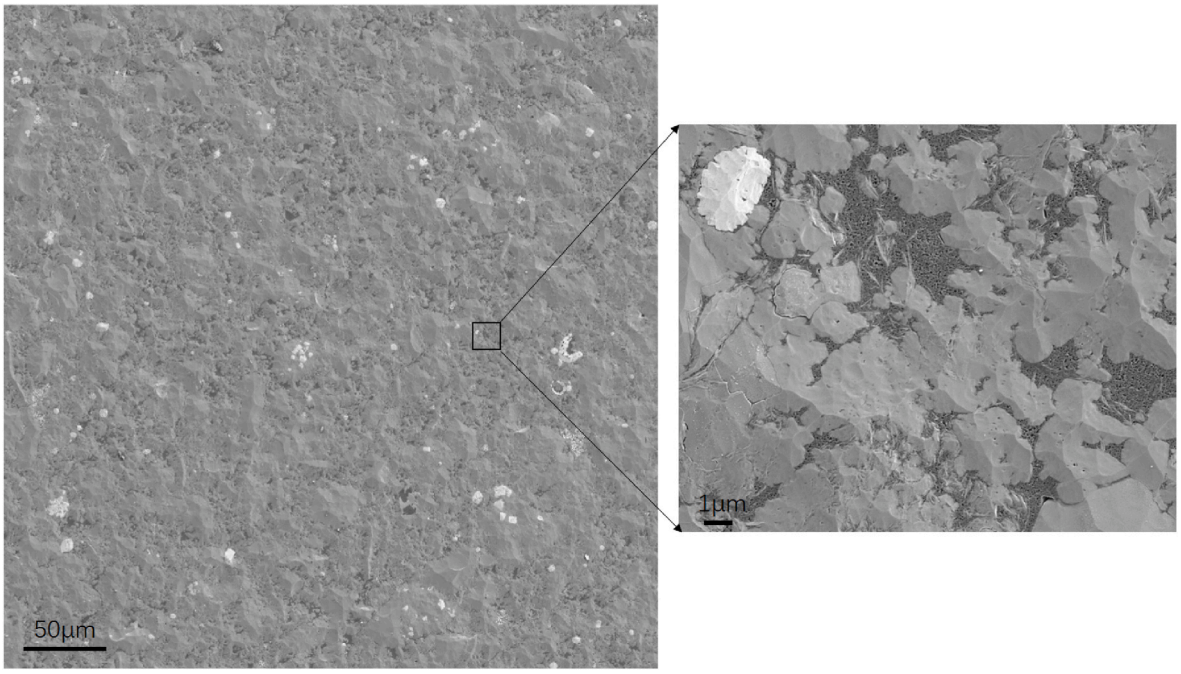

Fig. A3. Large area mosaic SEM imaging RS4-35JX.

4 Low Temperature Nitrogen Adsorption for Surface Area and Pore Size Distribution Analysis

A part of every shale sample was crushed and sieved between 20 and 40 Mesh screens to yield a sample with a diameter between 0.42 mm and 0.84 mm. Before analysis, the samples are dried and vacuumed at 110 °C for 4 h to fully exhaust the impurity gas and water content in the inner void space. The influence of the mesh size on the specific surface area (SSA) has ever been investigated. It is found that the SSAs of 8–20 Mesh and 20–40 Mesh samples are close, and the SSA will increase rapidly and beyond that of the core as the mesh number increases. The coarser the sample, the slower the adsorption rate due to its low-permeability characteristic, and the less possibility of weight loss during the vacuum process. The 20 to 40 Mesh is chosen to balance the experimental time consuming and the vacuum-induced weight loss.

About 1–3 g of this crushed and sieved sample is used to measure the low temperature nitrogen adsorption isotherm to determine the specific surface area and pore size distribution. Credited values for multi-point (MP) BET (Brunauer, Emmett and Telle) (Brunauer et al.) specific surface area measurements are determined by low-temperature nitrogen gas adsorption at liquid nitrogen temperature (77.3 K) using an automatic surface area and porosity analyzer (3H–2000PS1, Beishide Instrument).

Routine multi-point BET analysis method uses the data points pairs (p/p0 versus V, lower-left graph in Fig. A4) whose relative pressure (p/p0) is between 0.05 and 0.35 following Eq. (A3), and may lead to a negative C that is non-physical. To avoid this non-physical result, the upper pressure limit of data points used for linear fitting will be lowered until the BET constant C become positive.

$$\begin{cases} \dfrac{p/p_0}{V(1-p/p_0)} = \dfrac{C-1}{V_m C} p \Big/ p_0 + \dfrac{1}{V_m C} \\ S_w = 4.35 V_m \end{cases} \tag{A1}$$

where V is the adsorbed nitrogen amount (ml/g), p is the balance pressure (MPa), p_0 is the saturated vapor pressure, V_m is the single-layer adsorption volume (ml) under standard condition, S_w is the mass specific surface area (m^2/g) and C is the BET constant. The pore size distribution analysis is performed on the desorption branch of the isotherm with the BJH (Barrett-Joyner-Halenda) method The obtained bulk parameters are shown in Table A3.

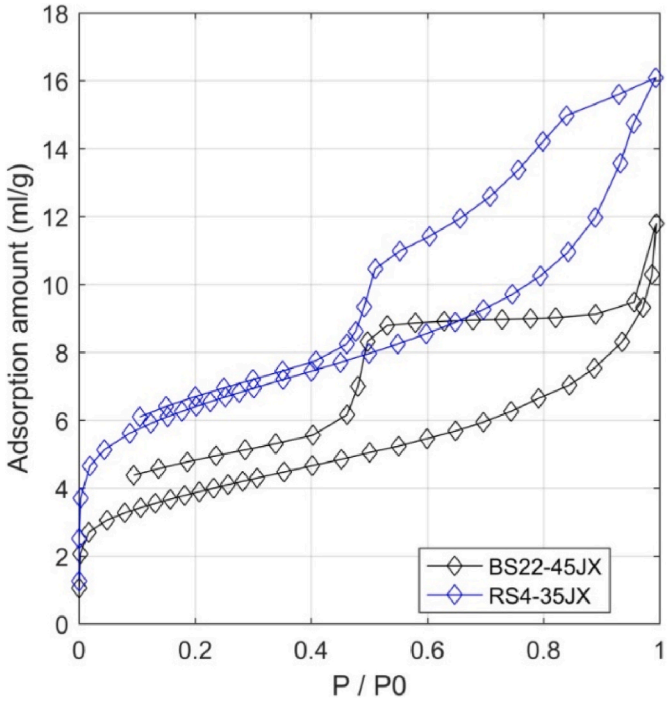

Fig. A4. Low temperature nitrogen adsorption isotherms of the studied samples

Table A1
Permeability from five consecutive tests of a sample close to sample BS22-45JX.

	Multiple-point BET specific surface area (m^2/g)	Cumulative pore volume by BJH analysis of the desorption branch (ml/g)
BS22-45JX	13.7	0.015
RS4-35JX	20.94	0.021

Where V is the adsorbed nitrogen amount (ml/g), p is the balance pressure (MPa), p_0 is the saturated vapor pressure, V_m is the single-layer adsorption volume (ml) under standard condition, S_w is the mass specific surface area (m^2/g) and C is the BET constant. The pore size distribution (PSD) analysis is performed on the desorption branch of the isotherm with the BJH method. The obtained bulk parameters are shown in Table A3.

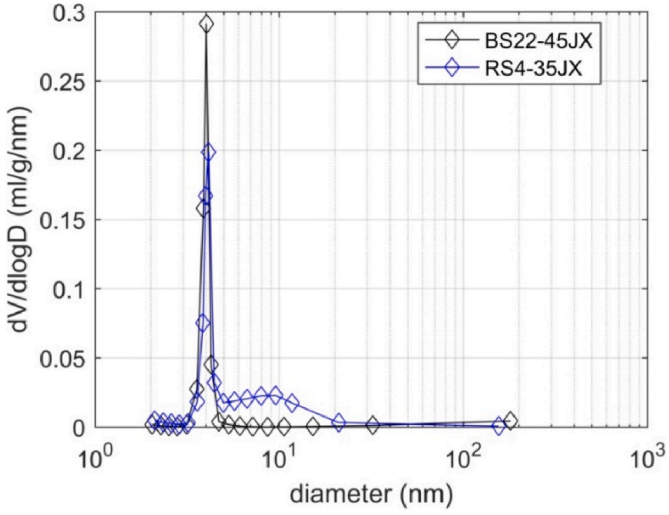

Fig. A5. PSD obtained with BJH method on desorption branch.

The hysteresis loop between adsorption and desorption branches indicates the existence of "ink bottle like model", in which a closed cavity if trapped by a narrow neck (Nguyen et al., 2011). The pore size distribution obtained with the desorption branch reflects more about the control of the pore space by the pore throat. There are two distinctly separate peaks (one is around 4 nm, another locates larger than 100 nm) in the PSD curve of BS22-45JX which have difference in magnitude. For the RS4-35JX, the two peaks are much closer with a broader distribution. The feature of pore structure inferred from the low temperature nitrogen adsorption experiment echoes the feature of crushed permeability.

4 Pressure Decay Curve of the Plug Sample

The pressure decay curves of the plug samples were also measured in the same in-house matrix permeameter and porosimeter as the crushed sample. Except for the sample drying time, which is extended to over 12 h to remove moisture more fully, the other parameter is consistent with the procedure that crushed sample used. The elapsed time for the BS22-45JX is much longer than that for the RS4-35JX sample.

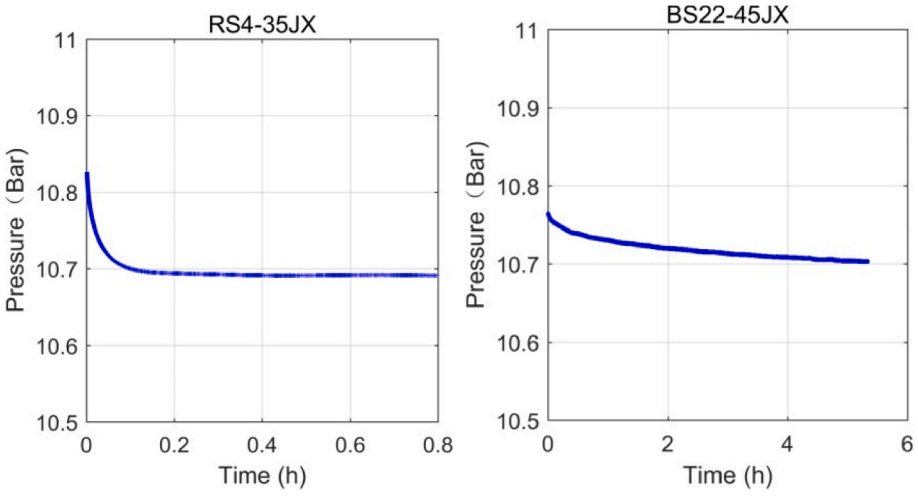

Fig. A6. Pressure decay curve of the plug samples.

5 Calculation of Basic Parameters

K_c is the ratio of the volume outside the sample including both reference chamber and sample chamber with respect to the pore volume of the samples, and can be calculated according to the following relationship.

$$K_c = \frac{V_b + V_s - V_{bulk}}{V_p} \tag{A2}$$

ρ_{c0} is the average gas density at the third step in Section 2.3, and can be calculated according to the following equation.

$$\rho_{c0} = \frac{\rho_1 V_b + \rho_0 (V_s - V_{sb} + V_p)}{V_b + V_s - V_{sb} + V_p} \tag{A3}$$

where ρ_1 is the gas density at pressure P_1 and can be determined according the equation of state of helium.

2 Further Variation of Permeability with Pressure

As the two studied samples have been crushed into particles smaller than the aperture of 20 Mesh screen, a sample that is close to BS22-45JX in the same well is tested at more pressures to further verify the relationship between permeability and pressure, coefficient of compressibility, C_g. It can be seen from Fig. A7 that the linear relationship between optimal permeability and P, C_g is stronger than that between curve fitting permeability and P, C_g when pressure is between 3 and 12 bars.

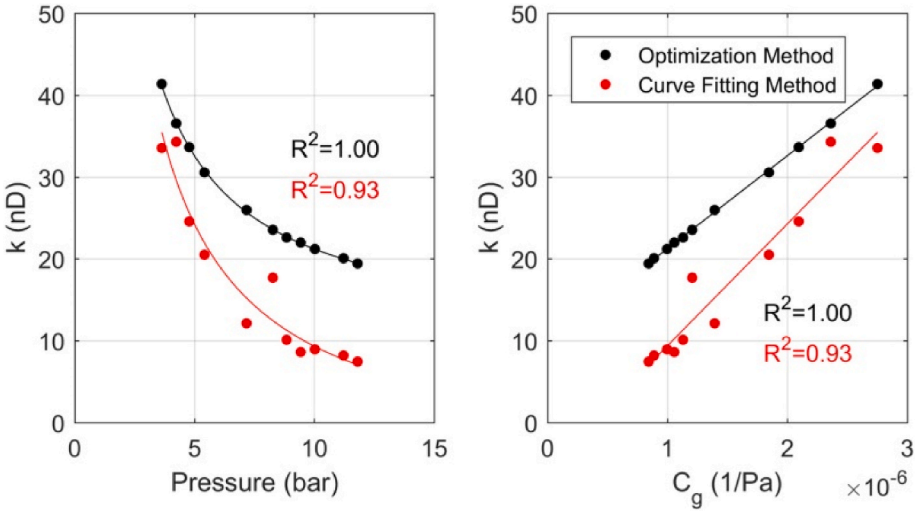

Fig. A7. Variations of permeability with P and C_g for a sample close to sample BS22-45JX.

3 Repeatability

As the two studied samples have been crushed into particles smaller than the aperture of a 20-Mesh screen, a sample that is close to BS22-45JX in the same well is further tested five times consecutively. From Fig. A8, it can be seen that although the final equilibration pressure is different, the $F_R(\tau)$ curves overlap. The optimal permeability is between 22.10nD and 23.53nD, while the curve fitting permeability is between 9.13nD and 11.34nD.

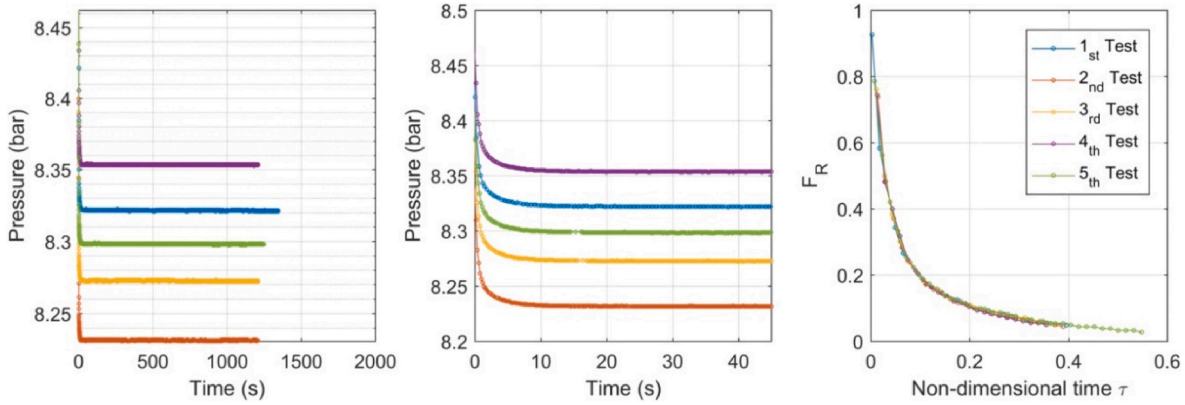

Fig. A8. Decay curves of P and F_R for 5 tests of a sample close to sample BS22-45JX.

Table A2
Permeability from five consecutive tests of a sample close to sample BS22-45JX.

	Porosity (%)	Curve Fitting Permeability (nD)	Optimal Permeability (nD)
1st	4.14%	9.68	22.43
2nd	4.11%	11.34	23.53
3rd	4.14%	10.39	22.72
4th	4.11%	11.05	22.10
5th	4.15%	9.13	22.69

References

Achang, M., Pashin, J.C., Atekwana, E.A., 2019. The influence of moisture on the permeability of crushed shale samples. Petrol. Sci. 16 (3), 492–501.
Achang, M., Pashin, J.C., Cui, X., 2017. The influence of particle size, microfractures, and pressure decay on measuring the permeability of crushed shale samples. Int. J. Coal Geol. 183, 174–187.
Cao, G., Lin, M., Ji, L., Jiang, W., Yang, M., 2019. Characterization of pore structures and gas transport characteristics of Longmaxi shale. Fuel 258, 116146.
Cao, G., Lin, M., Jiang, W., Zhao, W., Ji, L., Li, C., Lei, Da, 2018. A statistical-coupled model for organic-rich shale gas transport. J. Petrol. Sci. Eng. 169, 167–183.
Chavent, G., Dupuy, M., Lemmonier, P., 1975. History matching by use of optimal theory. Soc. Petrol. Eng. J. 15 (1), 74–86.
Civan, F., Devegowda, D., 2015. Comparison of shale permeability to gas determined by pressure-pulse transmission testing of core plugs and crushed samples. In: Proceedings of the 3rd Unconventional Resources Technology Conference.

Unconventional Resources Technology Conference. American Association of Petroleum Geologists, Tulsa, OK, USA. San Antonio, Texas, USA. 2015/7/20 - 2015/7/22.
Cui, G., Liu, J., Wei, M., Shi, R., Elsworth, D., 2018. Why shale permeability changes under variable effective stresses: new insights. Fuel 213, 55–71.
Cui, X., Bustin, R.M., Brezovski, R., Nassichuk, B., Glover, K., Pathi, V., 2010. A new method to simultaneously measure in-situ permeability and porosity under reservoir conditions: implications for characterization of unconventional gas reservoirs. In: Canadian Unconventional Resources and Canadian Unconventional Resources and International Petroleum Conference. Canadian Unconventional Resources and International Petroleum Conference. SPE, Calgary, Alberta. Canada. 2010/10/19 - 2010/10/21.
Cui, X., Bustin, A.M.M., Bustin, R.M., 2009. Measurements of gas permeability and diffusivity of tight reservoir rocks: different approaches and their applications. Geofluids 9 (3), 208–223.
Dadmohammadi, Y., Misra, S., Sondergeld, C.H., Rai, C.S., 2016. Simultaneous estimation of intrinsic permeability, effective porosity, PoreVolume compressibility, and klinkenberg-slip factor of ultra-tight rock samples based on laboratory pressure-step-decay method. In: SPE Low Perm Symposium. SPE Low Perm Symposium, Denver, Colorado, USA, 2016/5/5 - 2016/5/6. SPE.
Fathi, E., Tinni, A., Akkutlu, I.Y., 2012. Correction to Klinkenberg slip theory for gas flow in nano-capillaries. Int. J. Coal Geol. 103, 51–59.
Firouzi, M., Alnoaimi, K., Kovscek, A., Wilcox, J., 2014. Klinkenberg effect on predicting and measuring helium permeability in gas shales. Int. J. Coal Geol. 123, 62–68.
Fisher, Q., Lorinczi, P., Grattoni, C., Rybalcenko, K., Crook, A.J., Allshorn, S., Burns, A. D., Shafagh, I., 2017. Laboratory characterization of the porosity and permeability of gas shales using the crushed shale method: insights from experiments and numerical modelling. Mar. Petrol. Geol. 86, 95–110.
Handwerger, D.A., Suarez-Rivera, R., Vaughn, K.I., Keller, J.F., 2011. Improved petrophysical core measurements on tight shale reservoirs using retort and crushed samples. In: SPE Annual Technical Conference and Exhibition. SPE Annual Technical Conference and Exhibition. Denver, Colorado, USA. 2011/10/30 - 2011/11/2. SPE.
Haskett, S.E., Narahara, G.M., Holditch, S.A., 2013. A method for simultaneous determination of permeability and porosity in low-permeability cores. SPE Form. Eval. 3 (3), 651–658.
Heller, R., Vermylen, J., Zoback, M., 2014. Experimental investigation of matrix permeability of gas shales. Bulletin 98 (5), 975–995.
Hoang, T.G., Behrenbruch, P., Do Huu, P., 2017. Correction of laboratory gas permeability measurements using Klinkenberg-type correction models. The APPEA J. 57 (1), 171.
Javadpour, F., 2009. Nanopores and apparent permeability of gas flow in mudrocks (shales and siltstone). J. Can. Petrol. Technol. 48 (8), 16–21.
Ji, L., Lin, M., Jiang, W., Cao, G., Zhou, J., Luo, C., 2019. Investigation into the apparent permeability and gas-bearing property in typical organic pores in shale rocks. Mar. Petrol. Geol. 110, 871–885.
Jiang, W., Cao, G., Luo, C., Lin, M., Ji, L., Zhou, J., 2022. A composition-based model for methane adsorption of overmature shales in Wufeng and Longmaxi Formation, Sichuan Basin. Chem. Eng. J. 429 (6), 130766.
Jiang, W., Lin, M., Yi, Z., Li, H., Wu, S., 2017. Parameter determination using 3D FIB-SEM images for development of effective model of shale gas flow in nanoscale pore clusters. Transport Porous Media 117 (1), 5–25.
Li, J., Sultan, A.S., 2017. Klinkenberg slippage effect in the permeability computations of shale gas by the pore-scale simulations. J. Nat. Gas Sci. Eng. 48, 197–202.
Loucks, R.G., Reed, R.M., 2014. Scanning-electron-microscope petrographic evidence for distinguishing organic-matter pores associated with depositional organic matter versus migrated organic matter in mudrocks. GCAGS J. 3, 51–60.
Luffel, D.L., Guidry, F.K., 1992. New core analysis methods for measuring reservoir rock properties of devonian shale. J. Petrol. Technol. 44 (11), 1184–1190.
MA, X., Xie, J., Yong, R., Zhu, Y., 2020. Geological characteristics and high production control factors of shale gas reservoirs in Silurian Longmaxi Formation, southern Sichuan Basin, SW China. Petrol. Explor. Dev. 47 (5), 901–915.
Mehmani, A., Prodanović, M., Javadpour, F., 2013. Multiscale, multiphysics network modeling of shale matrix gas flows. Transport Porous Media 99 (2), 377–390.
Nguyen, P.T.M., Do, D.D., Nicholson, D., 2011. On the cavitation and pore blocking in cylindrical pores with simple connectivity. J. Phys. Chem. B 115 (42), 12160–12172.
Oliver, D.S., Chen, Y., 2011. Recent progress on reservoir history matching: a review. Comput. Geosci. 15 (1), 185–221.
Pan, Z., Connell, L.D., 2015. Reservoir simulation of free and adsorbed gas production from shale. J. Nat. Gas Sci. Eng. 22, 359–370.
Pan, Z., Ma, Y., Connell, L.D., Down, D.I., Camilleri, M., 2015. Measuring anisotropic permeability using a cubic shale sample in a triaxial cell. J. Nat. Gas Sci. Eng. 26, 336–344.
Peng, S., Loucks, B., 2016. Permeability measurements in mudrocks using gas-expansion methods on plug and crushed-rock samples. Mar. Petrol. Geol. 73, 299–310.
Profice, S., Lasseux, D., Jannot, Y., Jebara, N., Hamon, G., 2012. Permeability, porosity and Klinkenberg coefficient determination on crushed porous media. Petrophysics 53 (6), 430–438.
Qu, H., Pan, Z., Peng, Y., Zhou, F., 2016. Controls on matrix permeability of shale samples from Longmaxi and Niutitang formations, China. J. Nat. Gas Sci. Eng. 33, 599–610.
Tinni, A., Fathi, E., Agarwal, R., Sondergeld, C.H., Akkutlu, I.Y., Rai, C.S., 2013. Shale permeability measurements on plugs and crushed samples. In: SPE Canadian Unconventional Resources Conference. SPE Canadian Unconventional Resources Conference. Society of Petroleum Engineers, Calgary, Alberta. Canada. 2012-10-30.
Wu, J., Yuan, Y., Niu, S., Wei, X., Yang, J., 2020a. Multiscale characterization of pore structure and connectivity of Wufeng-Longmaxi shale in Sichuan Basin, China. Mar. Petrol. Geol. 120, 104514.
Wu, Y., Tahmasebi, P., Lin, C., Dong, C., 2020b. Process-based and dynamic 2D modeling of shale samples: considering the geology and pore-system evolution. Int. J. Coal Geol. 218, 103368.
Yang, B., Kang, Y., Li, X., You, L., Chen, M., 2017. An integrated method of measuring gas permeability and diffusion coefficient simultaneously via pressure decay tests in shale. Int. J. Coal Geol. 179, 1–10.
Zou, C., Dong, D., Wang, Y., Li, X., Huang, J., Wang, S., Guan, Q., Zhang, C., Wang, H., Liu, H., Bai, W., Liang, F., Lin, W., Zhao, Q., Liu, D., Yang, Z., Liang, P., Sun, S., Qiu, Z., 2015. Shale gas in China: characteristics, challenges and prospects (I). Petrol. Explor. Dev. 42 (6), 753–767.
Zou, C., Dong, D., Wang, Y., Li, X., Huang, J., Wang, S., Guan, Q., Zhang, C., Wang, H., Liu, H., Bai, W., Liang, F., Lin, W., Zhao, Q., Liu, D., Yang, Z., Liang, P., Sun, S., Qiu, Z., 2016. Shale gas in China: characteristics, challenges and prospects (II). Petrol. Explor. Dev. 43 (2), 182–196.